C-Pro: A coastal projector monitoring system using terrestrial photogrammetry with a geometric horizon constraint

E. Sánchez-García [a*], A. Balaguer-Beser [a,b] , J.E. Pardo-Pascual [a]

[a] Geo-Environmental Cartography and Remote Sensing Group, Department of Cartographic Engineering, Geodesy and Photogrammetry, Universitat Politècnica de València, Camí de Vera, s/n 46022, Valencia, Spain
[b] Department of Applied Mathematics, Universitat Politècnica de València, Camí de Vera, s/n 46022, Valencia, Spain
* Corresponding author. *E-mail address*: elena.sanchez.upv@gmail.com

ABSTRACT:

This paper describes a methodological protocol to project a terrestrial photograph of a coastal area – or whatever indicator is contained on it – in a georeferenced plane taking advantage of the terrestrial horizon as a geometric key. This feature, which appears in many beach photos, helps in camera repositioning and as a constraint in collinearity adjustment. This procedure is implemented in a tool called Coastal Projector (C-Pro) that is based on Matlab and adapts its methodology in accordance with the input data and the available parameters of the acquisition system. The method is tested in three coastal areas to assess the influence that the horizon constraint presents in the results. The proposed methodology increases the reliability and efficient use of existing recreational cameras (with non-optimal requirements, unknown image calibration, and at elevations lower than 7 m) to provide quantitative coastal data.

KEY WORDS: Beach monitoring, recreational cameras, coastal management, video-imaging system

1. Introduction

A proper management and planning of coastal areas is governed by an accurate understanding of these fragile and dynamic environments at different spatial and temporal scales. Modelling the coastline response to the effect of waves and sea level variation, especially in significantly unstable coasts such as sedimentary beaches, enables the evaluation of coastal retreat and coastline migration on large temporal scales. However, the complexity of the phenomena and processes that interact on the land-sea interface, makes this a deeply dynamic space in its form and arrangement (Boak and Turner, 2005). It is necessary to distinguish between oscillatory short-term effects and other long-term changes – and so monitoring changes at different temporal scales is helpful in a decision-making process involving environmental values and socioeconomic interests.

The spatial resolution and high temporal frequency achieved by terrestrial photogrammetric techniques have overcome the accuracy of other techniques in the field of monitoring. Techniques such as Airborne Light Detection and Ranging (LiDAR), Terrestrial Laser Scanner (TLS) and Global Positioning Systems in Real-Time Kinematic (RTK-GPS) define the shoreline and model the beach area with accuracy and reliability despite tedious fieldwork and costs. However, the high periodicity required to monitor dynamics in natural spaces is causing these techniques to be set aside. Conversely, remote sensing techniques are being used to establish and quantify erosion or accretion rates on beaches and the results are sufficiently accurate – in the order of several meters – to help in our understanding and prediction of long-term worldwide coastal evolution (Almonacid-Caballer et al., 2016). Nevertheless, its potential is reduced for local studies and short-term changes where video monitoring systems are consolidated as the current benchmark.

47   Terrestrial photogrammetric systems enable a systematic and continuous recording of the different actions
48   that take place in a specific coastal area. For instance, the local and rapid changes that occur during storms.
49   Some institutions have realized the need to establish a proper and integrated coastal zone management and
50   various video monitoring systems have been installed. The Argus system was the first developed for coastal
51   research (Holman et al., 1993) and was validated and widely used worldwide (Holman and Stanley, 2007).
52   Following the same principles, other coastal imaging systems were implemented. Archetti et al. (2008) made
53   a comparative study of four fixed-camera systems: Erdman (1998); Kosta (2006); Horus (2007); and
54   Beachkeeper (Brignone et al., 2012). Moreover, various works (Jiménez et al., 2007; Davidson et al., 2007;
55   Aarninkhof et al., 2003) widely recognize the success of video systems for coastal research and shoreline
56   monitoring through video-derived coastal indicators. Recent developments have emerged that access the
57   digital image data from non-expert systems and regardless of the camera technology (e.g.,Taborda and Silva,
58   2012; Kim et al., 2013).
59

60   Existing coastal imaging systems are ready focused and dedicated for a specific application and this leads to
61   some economic and positioning limitations. The measurement of shorelines, sand bars, beach widths, and
62   many other indicators is easy to accomplish using fixed cameras covering wide fields of view and located on
63   high elevation beach-front buildings. However, these optimal requirements are unusual on most beaches
64   around the world and so other approaches are being investigated.
65

66   Many recreational video-cameras are currently operating on the coastline and sending considerable data over
67   the internet - as well as a small number of systems designed by coastal managers in specific areas to control
68   storm events. Most of this data is captured by Surfcam stations whose main qualitative objective is to observe
69   breaking waves. As expected, the camera requirements are not optimal for quantitative measurements as they
70   are low-angle and single cameras mounted on low beachfront buildings and pointing nearly horizontal toward
71   the waves. Making the most of all the data from such shoreline monitoring cameras is the challenge tackled in
72   this paper and complementing other papers (Bracs et al., 2015) where the potential of Surfcam data has
73   already been proven through applying various solutions.
74

75   We propose a rigorous methodology – implemented in a coastal projector tool known as C-Pro – that
76   overcomes the photogrammetric difficulties and non-optimal conditions that are sometimes found in beach
77   photographs. The main goal is to use the terrestrial horizon as a photogrammetric constraint included in the
78   collinearity system to achieve a precise repositioning of the camera (Sánchez-García et al., 2015b). Van Den
79   Heuvel (1998) already advanced the benefits of using geometric constraints for object reconstruction. When
80   using a simple non-metric camera looking horizontally towards the coastline and from any elevation – even
81   from the ground where there is no other option – the horizon constraint helps the image spatial resection
82   system to converge on a precise solution that is valid for coastal monitoring. Moreover, because of the field of
83   view, most of the photos only show sand and water, and this makes it difficult to acquire ground control
84   points (GCP) with a suitable distribution to transform image information into real world coordinates.
85   Reducing the number of initial unknown parameters by adding horizon equations (Oreifej et al., 2011) would
86   be a great advantage in providing stability to the mathematical system.
87

88   Some works that use Surfcam online streaming images for measuring wave runup and intertidal beach
89   topography (Andriolo et al., 2016) are already taking advantage of C-Pro rectification methodology as the
90   horizon constraint is the key to achieving image calibration and a precise repositioning of the camera.
91

92   In this paper, Section 2 describes the different methodological steps depending on the number of parameters
93   initially known, access to camera calibration, knowledge of the initial location of the camera, or number of
94   available GCPs. Section 3 shows the results obtained after camera repositioning and image rectification
95   processes and shows the considerable advantages of incorporating the horizon constraint. Finally, Appendix A

presents the mathematical formulas necessary to incorporate horizon information in a monitoring system using terrestrial photogrammetry.

2. Methodology

2.1. A photogrammetric system

The analytical method consists of three main processes: calibration and image correction; repositioning of the camera; and image rectification. The followed protocol establishes a strong and rigorous geometric connection between both terrestrial and image spaces with the implementation of the horizon constraint in the collinearity system (described in Appendix A). Moreover, the tool will compute the adjustment adapting to different situations depending on the number of initially known and unknown external and internal orientation parameters.

2.1.1. Camera calibreation and image correction

In photogrammetry, the extraction of metric information requires a precise knowledge of the internal orientation parameters (IOP) – principal point coordinates $o=(x_0, y_0)$ and focal length (f) – and the distortion coefficients of the non-metric camera lens (assuming rectangular pixels skew factor is generally negligible). A camera acquires images composed of pixels where each pixel captures light traveling along the projection of a 3D ray. The projection rays in principle can be placed arbitrarily assuming the absence of a functional relationship between the projection rays and the pixels directed by the intrinsic parameters. Thus, the calibration is described in accordance with the coordinates of these rays (given in the local coordinate system) and the correspondence between the rays and pixels. After such calibration, each ray of the bundle passes correctly through the optical center.

In the present work, as we had access to the cameras, an a-priori laboratory study of the acquisition system itself was made. It is known that self-calibration can improve the accuracy of non-metric cameras (Chandler et al., 2005). This shows the potential that cheap cameras have for measuring surfaces when the lens model has been considered and a correct calibration of the intrinsic camera parameters has been made.

The calibration involves applying the Matlab camera calibration toolbox of Bouguet (2015). This calibration tool works with a series of images on a pattern like a checkerboard with the camera focused to infinity and taking the photos from different points of view and changing orientation and position. The IOP are estimated by an initial approach linearizing the equations and a least squares adjustment. These parameters are generally invariant and unique for each camera under similar conditions (Holland et al., 1997). Removing the induced effects of these intrinsic camera parameters, the image is corrected and undistorted by the empirical inverse model for compensating lens distortions proposed by Heikkila and Silvén, 1997. After the image correction, a correct geometric relation between the image and terrain systems will exist and the center of the undistorted image will coincide with the center of the original image – and will be consistent with the formulas shown in the following sections.

2.1.2. Camera repositioning

The process of determining the orientation parameters is understood as spatial resection and is considered as a particularization of a photogrammetric triangulation for a simple image. The six external orientation parameters (EOP) recreates the moment in which a photo is taken and defines the object coordinates of the camera center $\{X_{C_C}, Y_{C_C}, Z_{C_C}\}$, and its orientation angles $\{\omega, \varphi, \kappa\}$. Thus, it is necessary to establish a strong

144 and effective relation between the terrain and the image spaces before using the photos for photogrammetric
145 purposes.

146

147 The protocol carried out in the present work to calculate the orientation parameters follows one of two
148 methodologies - depending on the number of available GCPs (three being the minimum).

149

150 2.1.2.1. Direct Linear Transformation

151

152 Direct linear transformation (DLT) (Abdel-Aziz and Karara, 1971) is the most widely user linear camera
153 calibration method because of its simplicity (Bacakoglu and Kamel, 1997). DLT does not require initial
154 knowledge of the approximate orientation parameters because these are implicit in the 11 transformation
155 parameters. DLT theoretically adapts better to specific tasks, especially to close range photogrammetry –
156 which differs from our goals in coastal areas -. However, inside our protocol, DLT usefully provides the
157 initial approximated values for those unknown EOP in which the collinearity least squares fitting needs input
158 data to start. A great benefit of the DLT method is its linear quality regarding numerical problems that could
159 appear and we must be careful when the control points are coplanar because then the 11 transformation
160 parameters cease to be independent.

161

162 One control point with known terrain coordinates generates two linear equations which are expressed by the
163 following system of linear equations:

164
$$\begin{pmatrix} X\ Y\ Z\ 1\ 0\ 0\ 0\ 0\ -xX\ -xY\ -xZ \\ 0\ 0\ 0\ 0\ X\ Y\ Z\ 1\ -yX\ -yY\ -yZ \end{pmatrix} L = \begin{pmatrix} x \\ y \end{pmatrix} \ \rightarrow A\,L = \begin{pmatrix} x \\ y \end{pmatrix} \quad (1)$$

165

166 being $L = (L_1, L_2, L_3, L_4, L_5, L_6, L_7, L_8, L_9, L_{10}, L_{11})^T$. An overdetermined set of linear equations: $M\,L = N$ is
167 obtained by applying (1) for a minimum of six GCPs. We can then obtain L using the least square method.

168

169 The current relation between these 11 DLT parameters, *L*, and the other 9 (internal and external camera
170 parameters) of the collinearity equations is well-known (Seedahmed and Habib, 2002). If it is possible to
171 establish the internal parameters as a result of the camera calibration, or if the camera position is available,
172 then it would be preferable to use these. Moreover, when the horizon appears in the photo, the values obtained
173 by DLT will not be used as initials, because we would prefer those obtained by (A.26) and (A.27) – described
174 at the end of appendix A.

175

176 2.1.2.2. Refinement process by collinearity

177

178 To guarantee a strong relationship between terrain and image spaces, an iterative adjustment system must be
179 carried out to obtain the parameters that recreate the time of the shoot as faithfully as possible. This point of
180 the mathematical process is where it is necessary to introduce a geometric constraint to add methodological
181 rigor. Photographs of a beach area usually present homogeneous characteristics that hinder a proper
182 distribution of the GCPs. However, the horizon curve is an essential strategic element. In this locus, all
183 vanishing points of the image converge and therefore it acts as if we had a set of control points at infinity.
184 Appendix A describes the details of a mathematical procedure for having characterized the horizon, relating it
185 to the EOP by means of (A.22). Our methodological protocol proposes the inclusion of these novel constraints
186 in the adjustment to obtain a much more accurate solution.

187

188 All iterative adjustment starts from an initial approximate solution of all the parameters. The prior values for
189 the internal parameters can correspond with those obtained by DLT, or by the camera calibration process.
190 Depending on the reliability of these initial parameters, the collinearity will then be resolved and so free all

191   the parameters if they are from DLT, or freeing only six because the IOP will remain fixed (providing they
192   are produced after calibration and are accurate enough).

193

194   The initial camera position coordinates are obtained by the camera user, but in cases where this is not possible
195   they are approximated by the DLT method. When the horizon appears in the image, initial orientation
196   parameters, $\{\omega, \varphi, \kappa\}$, are computed by means of (A.26) and (A.27). In other cases, those values are also
197   obtained by the DLT.

198

199   The resolution of the spatial resection by the collinearity condition is carried out developing the classical non-
200   linear equations of the central projection which relates the position of the GCP, (X,Y,Z), in the object space of
201   the position of its image point (x,y) in the image plane.

202

203   In this paper, we propose to include the geometric horizon constraint in the refinement adjustment, using the
204   mathematical procedure described in Appendix A. Thus, we consider equations (A.22) and we define the
205   following functions:

206

207
$$
\left.\begin{array}{l}
F_{H\xi}(\omega, \varphi) = \arccos(\cos(\varphi)\cos(\omega)) - \xi \\
F_{H\psi}(\omega, \varphi) = \arctan\left(\dfrac{-\sin(\varphi)}{\cos(\varphi)\sin(\omega)}\right) - \psi
\end{array}\right\} \quad (2)
$$

208

209   considering that ψ and ξ are defined constants, respectively, by means of (A.1)-(A.3) and (A.12), using the
210   horizon information through the marked points A, B, and C in the image. Thus, we add to the collinearity
211   system these two new linearized equations:

212
$$
\begin{pmatrix} F_{H\xi} \\ F_{H\psi} \end{pmatrix}_0 + \begin{pmatrix} \dfrac{\partial F_{H\xi}}{\partial \omega} & \dfrac{\partial F_{H\xi}}{\partial \varphi} & 0 & 0 & 0 & 0 & 0 & 0 & 0 \\ \dfrac{\partial F_{H\psi}}{\partial \omega} & \dfrac{\partial F_{H\psi}}{\partial \varphi} & 0 & 0 & 0 & 0 & 0 & 0 & 0 \end{pmatrix}_0 \begin{pmatrix} d\omega \\ d\varphi \\ d\kappa \\ dX_{C_C} \\ dY_{C_C} \\ dZ_{C_C} \\ dx_0 \\ dy_0 \\ df \end{pmatrix} = \begin{pmatrix} 0 \\ 0 \end{pmatrix} \quad (3)
$$

213

214   If the IOP have been computed by calibration, the refinement process only aims to obtain the correction for
215   the six EOP $\{d\omega, d\varphi, d\kappa, dX_{C_C}, dY_{C_C}, dZ_{C_C}\}$. By applying collinearity with a minimum of three GCP, a
216   system formed by those classical collinearity equations together with (3) will then be solved. However, if the
217   correction of the three IOP $\{dx_0, dy_0, df\}$ also needs to be computed, then the tool will solve collinearity
218   for nine parameters requiring at least four GCP. This case occurs when the IOP come from DLT. The whole
219   spatial resection system will be expressed as,

220

221   B (dP) = K   (4)
222   being:

223    $dP = \left(d\omega, d\varphi, d\kappa, dX_{C_C}, dY_{C_C}, dZ_{C_C}\right)^T$ or $dP = \left(d\omega, d\varphi, d\kappa, dX_{C_C}, dY_{C_C}, dZ_{C_C}, dx_0, dy_0, df\right)^T$

224

225   considering the appropriate number of GCP for each of the situations commented above. System (4) will be
226   resolved by the weighted least square method whose solution gives us the parameter correction:

227

228                    $dP = (B^T W B)^{-1} B^T W K$ (5)

229
230   where W is the diagonal weight matrix. The weight assigned to the classical collinearity equations is the same
231   for all, but can vary depending on the reliability associated by the user with each of the GCP. As equations (3)
232   should act as a constraint to the fitting, the weights assigned to these equations in our methodology are much
233   higher than those used for the equations related to GCP. We will study the influence of those weights in
234   Section 4. As a consequence, an accurate determination of the initial points to form the horizon approximation
235   is important. In the results section, some performances analyze how the weight of the horizon equations
236   influence in the resection adjustment.

237

238   We will consider an iterative process solving each step of the system (4) considering the parameters computed
239   with the correction of the above iteration. Thus, in (4) B and K are defined in the k-iteration ($k \geq 1$) using the
240   solution obtained in the *(k-1)*-iteration so:

241

242    $\left(\omega^k, \varphi^k, \kappa^k, X_{C_C}{}^k, Y_{C_C}{}^k, Z_{C_C}{}^k, x_0{}^k, y_0{}^k, f^k\right)=$

243    $$\begin{pmatrix} \omega^{k-1} + d\omega^{k-1}, \varphi^{k-1} + d\varphi^{k-1}, \kappa^{k-1} + d\kappa^{k-1}, X_{C_C}{}^{k-1} + dX_{C_C}{}^{k-1}, Y_{C_C}{}^{k-1} + dY_{C_C}{}^{k-1}, \\ Z_{C_C}{}^{k-1} + dZ_{C_C}{}^{k-1}, x_0{}^{k-1} + dx_0{}^{k-1}, y_0{}^{k-1} + dy_0{}^{k-1}, f^{k-1} + df^{k-1} \end{pmatrix} \qquad (6)$$

244   That process finishes when each of the correction parameters becomes insignificant (the established threshold
245   is equal to 10^{-10}).

246

247   To establish the convergence of the system, at the beginning of the k-iteration, ($k \geq 1$), the C-Pro tool will
248   color in green the calculated image coordinates of the GCP by computing (x,y) by means of the collinearity
249   equations, considering the parameters obtained using (6) and the (X,Y) coordinates of each GCP. Moreover,
250   the horizon line will be approximated considering:

251

252    $$d^k_{horizon} = -f^k * \tan\left(\arccos\left(\cos(\varphi^k)\cos(\omega^k)\right) - \arccos\left(\frac{Z_{C_C}{}^{k}+0.42*\frac{(D^k)^2}{Rt}}{D^k}\right)\right) \qquad (7)$$

253

254   where D^k is defined by means of (A.10) considering $Z_{C_C}{}^k$ defined by (6), and:

255

256    $$\psi^k_{calc} = \arctan\left(\frac{-\sin(\varphi^k)}{\cos(\varphi^k)\sin(\omega^k)}\right) \qquad (8)$$

257

258   using the following equation:

259

260    $$y = y_0^k + d^k_{horizon}\cos(\psi^k_{calc}) - \tan(\psi^k_{calc})\left(x - x_0^k - d^k_{horizon}\sin(\psi^k_{calc})\right) \qquad (9)$$

261

262   Thus, the horizon line is recomputed in each iteration with the newest parameters until the adjustment process
263   ends.

264

265   **2.1.3. Image rectification and data extraction**

266

267   Once the repositioning camera has been fruitfully achieved, the rectification process can be done. In our tool,
268   the user can choose whether to project a piece of the image or just an element contained therein over a
269   specific plane with a known Z_T value.

270

271 Choosing the first option, the tool detects the image limits in terrain coordinates and a georeferenced grid is
272 created for a specific pixel size on the specific Z_T. Each pixel is then filled by an image intensity value
273 through inverse mapping techniques and using the nearest neighbor interpolation method. In this case, the
274 final product is a rectified georeferenced image (Tiff World File) used by standard GIS applications.
275
276 Nevertheless, by following the second option, the user can digitalize a specific feature of interest as a coastal
277 indicator – such as an established shoreline, the landward edge, the foredune toe, the cliff top – or just upload
278 a file with the image coordinates that the C-Pro tool is expected to project. This coordinate rectification is
279 then either done by collinearity equations or by the DLT – both methods lead to the same solution. In the last
280 case, we have to convert the camera's internal and external parameters to the characteristic's 11
281 transformation parameters of DLT which satisfy equations (1). From the DLT equations we can obtain the
282 planimetric terrain coordinates (X, Y) projecting the image coordinates (x, y) of the indicator of interest on a
283 specific Z_T, considering the next linear equation system (10).
284

285
$$\begin{cases} (L_5 - L_9 y)X + (L_6 - L_{10} y)Y = (L_{11} y - L_7)Z_T + y - L_8 \\ (L_1 - L_9 x)X + (L_2 - L_{10} x)Y = (L_{11} x - L_3)Z_T + x - L_4 \end{cases} \qquad (10)$$

286
287 It is interesting to note the importance of the Z_T projection value because only the points located at this same
288 elevation will be projected at the correct place. The remainder points will be displaced unless we project the
289 photography over a digital terrain model supporting each pixel of the image with its associate altitudinal
290 value. In this paper the photographs are projected above the mean sea level (Z_T=MSL) because the key image
291 feature to be correctly georeferenced is the shoreline. However, in order to know the errors of the image
292 rectification process, some terrain points have been projected over its associated altimetric coordinate
293 (measured by RTK-GPS) and assessed its positional accuracy by solving (12).
294
295 **2.2. Practical implementation of C-Pro**
296
297 This section shows the main steps in the implementation of the C-Pro.
298
299 **Step 1: Calibration and image correction.**
300
301 1a) **With calibrated IOP:** If we have access to the cameras then we compute the IOP – principal point
302 coordinates $O = (x_0, y_0)$ and focal length (f) – by image calibration. **With unknown IOP:** In the other cases,
303 having at least six GCPs, the system calculates an IOP estimation by direct linear transformation (DLT).
304
305 1b) The image is corrected and undistorted by the empirical inverse model for compensating lens distortion
306 described in Bouguet (2015).
307
308 **Step 2: Repositioning of the camera through the spatial resection process.**
309
310 2a) Initial camera position $\{X_{C_C}, Y_{C_C}, Z_{C_C}\}$ is estimated by the user. However, when it is not possible, C-Pro
311 will offer a first approximation of this through the DLT method (Section 2.1.2.1).
312
313 2b) **With horizon constraint (with HC):** If the horizon appears in the image then, angle ψ is defined by
314 means of (A.1) (case two points) or (A.2)-(A.3) (case three points). Moreover, ξ is computed using (A.12)
315 through the marked horizon points in the image and considering the focal length (f) obtained in step 1 and the
316 camera center elevation Z_{C_C} defined in 2a). $\{\omega, \varphi, \kappa\}$ are then computed by means of (A.26) and (A.27).

317 **Without horizon constraint (without HC):** in cases where the horizon equation is not available, $\{\omega, \varphi, \kappa\}$
318 are estimated by the DLT.

319

320 2c) C-Pro calculates the final EOP through an iterative weighted least squares fitting (5) over the linearized
321 collinearity equations (two equations for each GCP), which starts with the parameters defined in 2b) and
322 finishes when each of the correction parameters become less than 10^{-10}. The weight assigned to those
323 equations is equal to 1, but can vary depending on the reliability associated by the user to each of the GCP.
324 Moreover, in the cases with horizon constraint, the linearized horizon constraints (3) are added with an
325 associated weight of 10^{12} to solve the photo geometry. The system will be resolved and freeing all parameters
326 if the IOP in step 1 proceeds from DLT (with unknown IOP), or freeing only six of them when the IOP
327 remains fixed by considering that they are computed in step 1 (with calibrated IOP).

328

329 2d) To discover how the convergence of the system is progressing, C-Pro colors green (at the end of each
330 iteration) the calculated image coordinates of the GCP by computing (x,y) by means of the collinearity
331 equations and considering the parameters obtained using (6). Moreover, the horizon line is also colored in
332 green considering equation (9).

333

334 **Step 3: Image rectification**

335

336 3a) To project a piece of the image on a specific plane with a known Z_T value, a georeferenced grid is created
337 and each pixel is filled with an image intensity value through inverse mapping techniques and using the
338 nearest neighbor interpolation method.

339

340 3b) Collinearity equations or the DLT equations given in (10) will be used to project an element contained in
341 the image on a plane with a constant Z_T coordinate. In the case of shoreline rectification, the MSL value is
342 used as Z_T.

343

344 **3. Testing of the horizon constraint and C-Pro software**

345

346 Assessing the protocol proposed in this paper, the following subsections show the benefits achieved by
347 including the horizon constraint in the spatial resection process.

348

349 The analyses are carried out in the three coastal areas described in this section and working with specific
350 photogrammetry conditions that must be solved. The tests are made with non-fixed cameras. Therefore, in the
351 first step of C-Pro, the IOP of the acquisition system was obtained through image calibration (Bouguet, 2015).
352 However, some of the results of this section will be obtained when considering the IOP as unknown to prove
353 that C-Pro also works accurately in such cases.

354

355 **3.1. Data and study area**

356

357 The analyses are carried out in three coastal areas. Two are in the region of Valencia on the Mediterranean
358 coast (Spain) and are long micro-tidal beaches (tide regime is less than 0.18 m) with low and sandy coastlines
359 and a wide shoal. Patacona beach and El Saler beach are popular with tourists and have suffered a marked
360 erosion in recent decades due to sand retention by the jetties of the port of Valencia – north of El Saler beach
361 – that interrupts the littoral drift (Sánchez-García et al., 2015a). The third study area is Magoito beach, located
362 in Sintra, on the Atlantic coast of Portugal. This is a mesotidal beach (tide range between 2 and 3 m) with a
363 long stretch of golden sand dotted with numerous rocks and imposing cliffs that rise from the beach.

364

365 A photogrammetric analysis in the study area was carried out by simple non-fixed cameras. In the Valencian
366 beaches the images were taken with a digital single-lens reflex camera (SONY DSLR-A330) whereas a
367 Mobotix MX-M12D camera was used at Magoito. The zoom lens is fixed to infinity and care was taken to
368 ensure that the photos do not blur. Furthermore, to achieve the different assessments shown in this paper, it
369 was necessary to ensure that the terrestrial horizon appears in the photo, at least partly, as well as a minimum
370 of six non-coplanar GCPs that are well spread out and clearly and unequivocally displayed (Sánchez-García et
371 al., 2016). These theoretical conditions hardly ever occur because of the homogeneous media found on
372 beaches, where most of the photo shows water and sand. Moreover, because GCPs generally cover a very
373 small part of the whole picture, infinite control points representing the terrestrial horizon and located far from
374 the camera help resolve the photogrammetric problem.
375
376 Concerning RTK-GPS data, existing terrain points were measured accurately in several previous field
377 campaigns and acted as GCPs by solving the geometry of the photo through the link between image and
378 terrain systems – or only as checkpoints for assessing the solvency of that photogrammetric solution and
379 image rectification. The stability of these points was ensured during all the evaluation process. The camera
380 coordinates were also acquired by GPS to subsequently measure the error obtained in camera positioning. The
381 planimetric coordinates (XY) and orthometric altitudes (Z) are accurate to less than 2 cm in planimetry and
382 within 4 cm in altimetry (referenced respectively in the UTM projection – GRS80 – and the EGM08 geoid
383 model).
384
385 Magoito beach is a study area with good characteristics for the usual photogrammetry requirements. It was
386 possible to locate the camera in a high place – an elevation of 35.6 m –, where a broad view of the beach area
387 is seen and the horizon covers the entire width of the image (see Fig. 1). Moreover, during low tide it was
388 possible to obtain 28 GPS points by taking advantage of some rocky elements that remained in sight. The
389 distribution of these points through the target area – in this case generally centered in front of the camera –
390 will condition the significance of the positional error, as we will see in the results section when we must
391 distinguish between both longitudinal and cross-shore components of error.
392
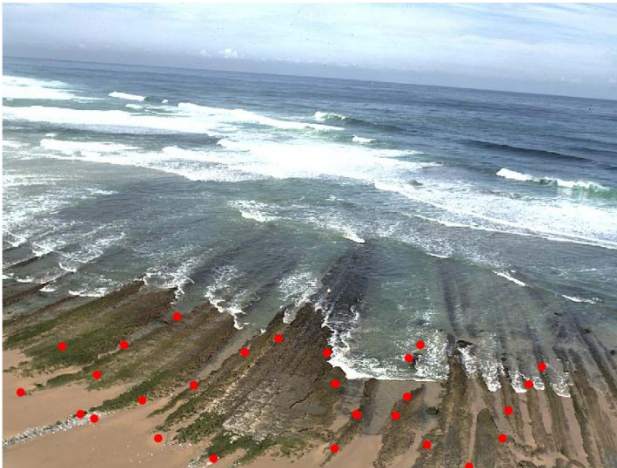
394 Fig. 1. Photo taken on Magoito beach at low tide. The GPS points (GCP and checkpoints) are shown in red.
395
396 Secondly, the coastal photos at El Saler beach were taken from two non-fixed camera positions at the top of a
397 43 m high building but separated from the shore by around 230 m (a park with protected coastal dunes being
398 between the building and the coast). Consequently, the shoreline is partially hidden in the photos. We call the
399 shots CS or CN depending on the camera location on the south or north side of the building from where three
400 and four photographs were taken respectively each day. From a specific position, the photos were taken

sequentially turning from north to south and numbering them by order. CN1 and CS1 photos capture almost the same target area but from another camera position. Moreover, depending on the photo orientation, the extent of horizon seen in the photos changes and we will analyze this in the results section to establish how this influences the horizon approximation formulas. Differences regarding the extent of the horizon are obvious in Fig. 2 depending on the existence of elements that hide it – such as the Port of Valencia in the northern part (CN1) and, to a lesser extent, the Cullera headland to the south (CS3). GPS points were measured along the entire area (about one kilometer long) and these points were included in photos that took advantage of fixed elements – outside the beach area – such as parking borders and pedestrian walkways.

The photogrammetric field campaigns were made during two days, 25 May and 17 June 2016, when the water/land border was measured (using RTK-GPS to record automatic coordinates every second). The availability of this data enables us to make comparisons with other digitized shorelines for the resulting and rectified photos and assess accuracy.

Fig. 2. Three examples of photos at El Saler beach taken from different camera position on 17 June 2016; the first photo from the north camera (NC) and the other two from the south camera (CS). Distribution of the GPS points in the area is dotted in red and the horizon line is shown in blue. CN1 is an example of where the horizon formulas are obtained by two points, while CS2 and CS3 are obtained by three points.

Finally, the third study area is Patacona beach where an additional longshore assessment was made on 22 September 2015. The photogrammetric procedure was performed twice – from same camera position but at different elevations – pointing north and south (changing the camera position). Taking advantage of a gangway near the shore, the photos were taken using a tripod (Z_{C_C}=4.7 m) to hold the spatial resection of the camera. However, photos were then carefully taken from a handheld camera at the top of a stepladder (Z_{C_C}=6.8 m). Consequently, we have different solutions of the camera spatial resection for each image. Given the absence of fixed elements in the beach area, several surveying rods were used as GCPs (black points on the map and photos in Fig. 3), producing a maximum of six and nine GCPs respectively for the northern and southern photos.

The main goal of the experiment carried out in this area was to understand the functioning of our methodology when camera elevation is reduced. Moreover, to measure the longshore error after image rectification, a field campaign took a set of photos coincident in time with the data acquisition every 20 m for two or three GPS trackers. These devices were separated some 2 m apart and measured moving checkpoints for a distance of 280 m from the camera. We had to establish a distance limit because of the subsequent difficulties in the detection of those checkpoints in the image. Fig. 3 exemplifies the experiment performed showing a photo of the north beach and of the south beach where respectively the positions (checkpoints) of three and two GPS trackers are detected. We can also see that the horizon appears in less than half the image and so the horizon approximation formula uses two points.
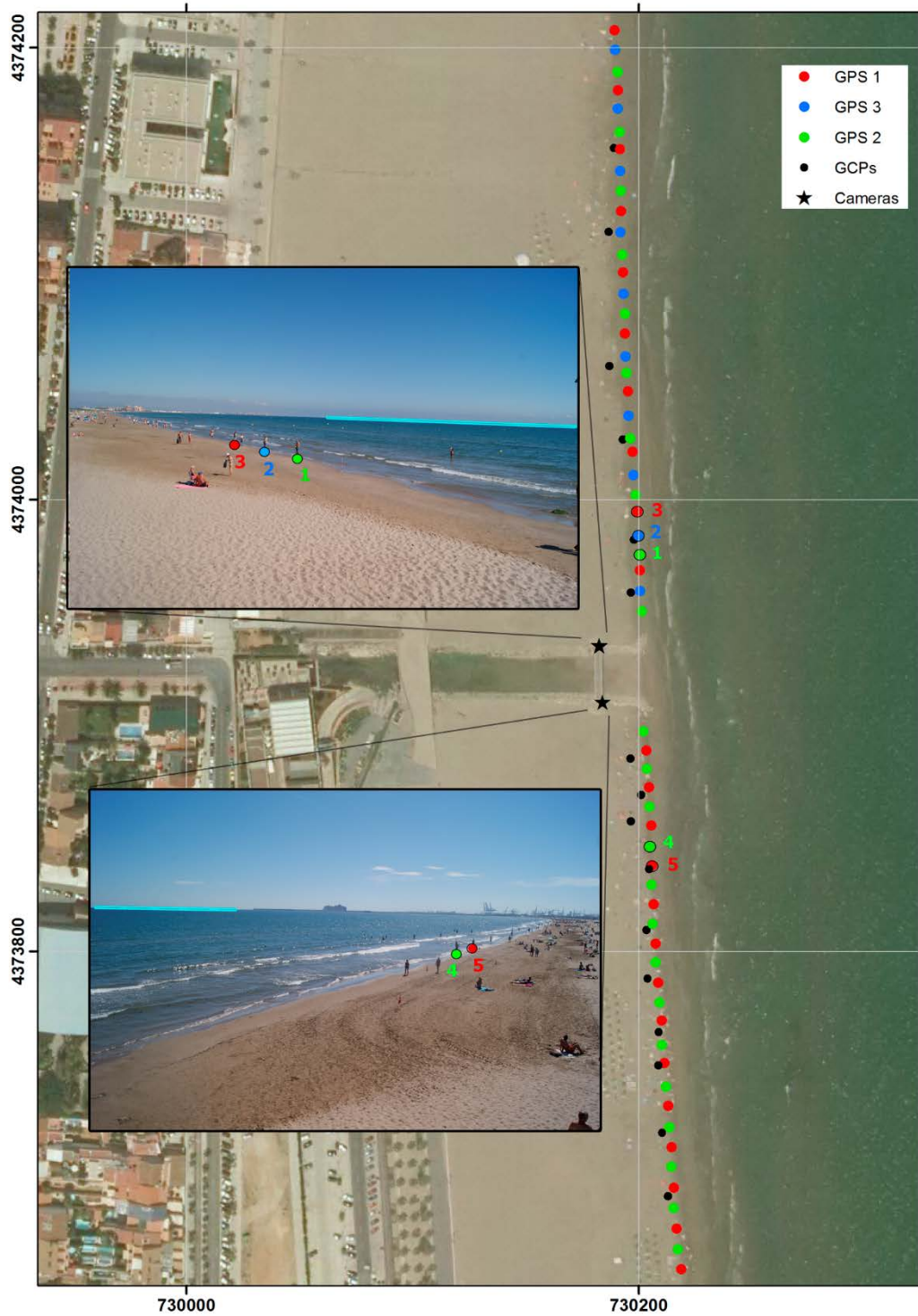
Fig. 3. Mapping GPS data (GCPs and shoreline checkpoints) and two examples of photos acquired for the assessment at Patacona beach. This figure shows the procedure carried out where each shot is performed at the same time as the GPS trackers (three for the north and two for the south) record shoreline positions (checkpoints tagged and numbered) and subsequently evaluated on the rectified photos. The extension of a usable horizon is marked with a blue line. Grid coordinates: GCS_ETRS89 UTM.

3.2. Improvement of camera positioning by adding the horizon constraint regardless of whether IOP is known or not

The aim of this subsection is to establish the improvements and differences achieved by the influence of the horizon constraint in the spatial resection procedure (results of step 2c). For this reason, the resulting performances are achieved by applying C-Pro in various ways, that is, setting and not setting the IOP (depending on whether these are considered as unknown or known) and with and without including the horizon equations in the fitting.

Validating the final EOP for each test at Magoito and Patacona beaches, Table 1 summarizes the differences between these resulting camera coordinates against those accurately measured by GPS. To clarify, the camera positioning error is:

$$Camera\ positioning\ error\ (CPE) = \sqrt{\left(X_{Cc_{GPS}} - X_{Cc}\right)^2 + \left(Y_{Cc_{GPS}} - Y_{Cc}\right)^2 + \left(Z_{Cc_{GPS}} - Z_{Cc}\right)^2} \qquad (11)$$

being $\{X_{C_C}, Y_{C_C}, Z_{C_C}\}$ and $\{X_{Cc_{GPS}}, Y_{Cc_{GPS}}, Z_{Cc_{GPS}}\}$ the camera position coordinates obtained by C-Pro and RTK-GPS techniques respectively.

		CPE (m)		
		Without horizon constraint	With horizon constraint	
			Case two points	Case three points
Magoito beach	With calibrated IOP	1.517	1.037	0.972
	With unknown IOP	19.780	1.848	1.827
Patacona beach	With calibrated IOP	0.847	0.566	-
	With unknown IOP	3.395	0.742	-

Table 1. CPE (m) achieved using (11) at Magoito and Patacona beaches. Errors are obtained by comparing the camera position coordinates calculated by C-Pro against those measured by GPS. Results for Patacona beach are the average values in each assessment from all errors shown in Fig. 4.

It is observed that when the camera elevation is higher – as occurs in Magoito with a camera elevation of 35.6 m in comparison with the elevation of Patacona that ranges from 4.7 or 6.8 m – the uncertainty of the IOP causes system inconsistency and overstated positioning error. Results of Table 1 reveal the usefulness of the horizon constraint in step 2 of C-Pro. For both cases, with calibrated and unknown IOP, the horizon improves the convergence. However, it is in this last case when it becomes even more necessary to use the horizon to obtain a usable camera position. Regarding the differences between both horizon approximations, the Magoito beach image has a full view of the horizon and the approximation achieved by three points forming a circumference leads to slightly better results. At Patacona beach, the horizon curve is built from only two points because the horizon is just seen in half of the photo and, consequently, its definition using three nearby points would not be rigorous.
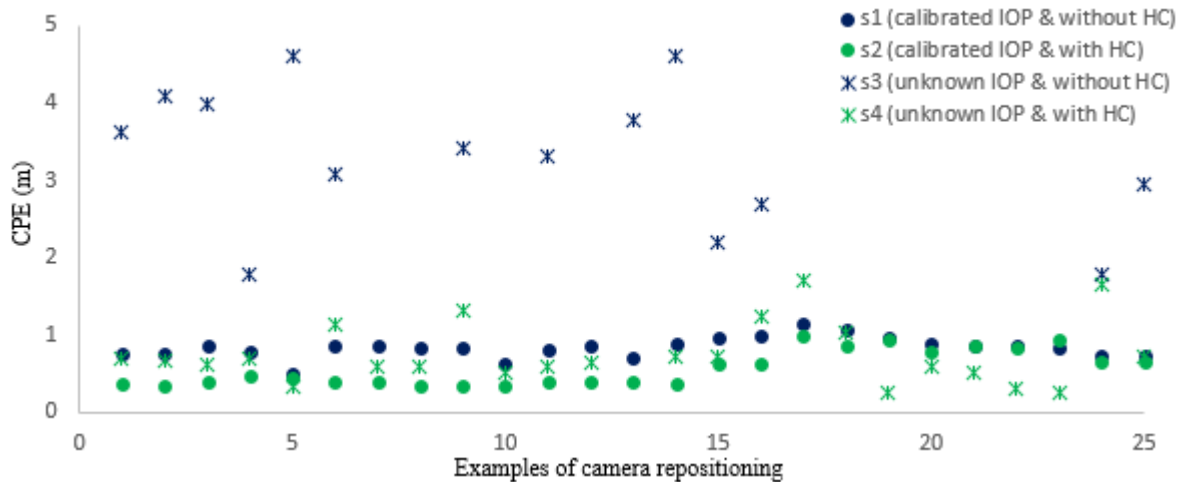
Fig. 4. CPE obtained using (11) for 25 different performances and calculated following four different procedures for Patacona beach. Green indicates the use of the horizon constraint in the adjustment, whereas blue represents its absence. Moreover, the asterisks represent those results where the adjustment is made using free IOP and the dots where IOP are obtained by camera calibration.

Fig. 4 shows the results obtained for the 25 performances at Patacona beach where the least squares solution from step 2 of C-Pro has converged. CPE verifies the usefulness of including the horizon constraints (A.26)-(A.27) and (3) to obtain an accurate solution for the camera location regardless of whether the IOP are known by calibration or not. It is noteworthy that in most cases when the IOP are unknown, the system solution does not converge unless we introduce the equations of the horizon constraint. In other cases, although the system converges, the achieved solution is not useful and the horizon equations help to obtain it with greater accuracy with errors of within 2 m in camera position (results of s4 in Fig. 4).

Therefore, thanks to the methodology implemented in this paper, and despite photogrammetry weaknesses when the IOP are unknown, spatial resection of C-Pro achieves accuracies that are in the range of those obtained when all the parameters are under control – an average CPE of 0.742 m versus 0.566 m respectively. However, the magnitude of this error is going to be strongly related with other conditioning factors. The main factors are: the GCP distribution; the degree of success produced during the detection in the photo of GCPs and horizon points; and the difficulties in image geometry.
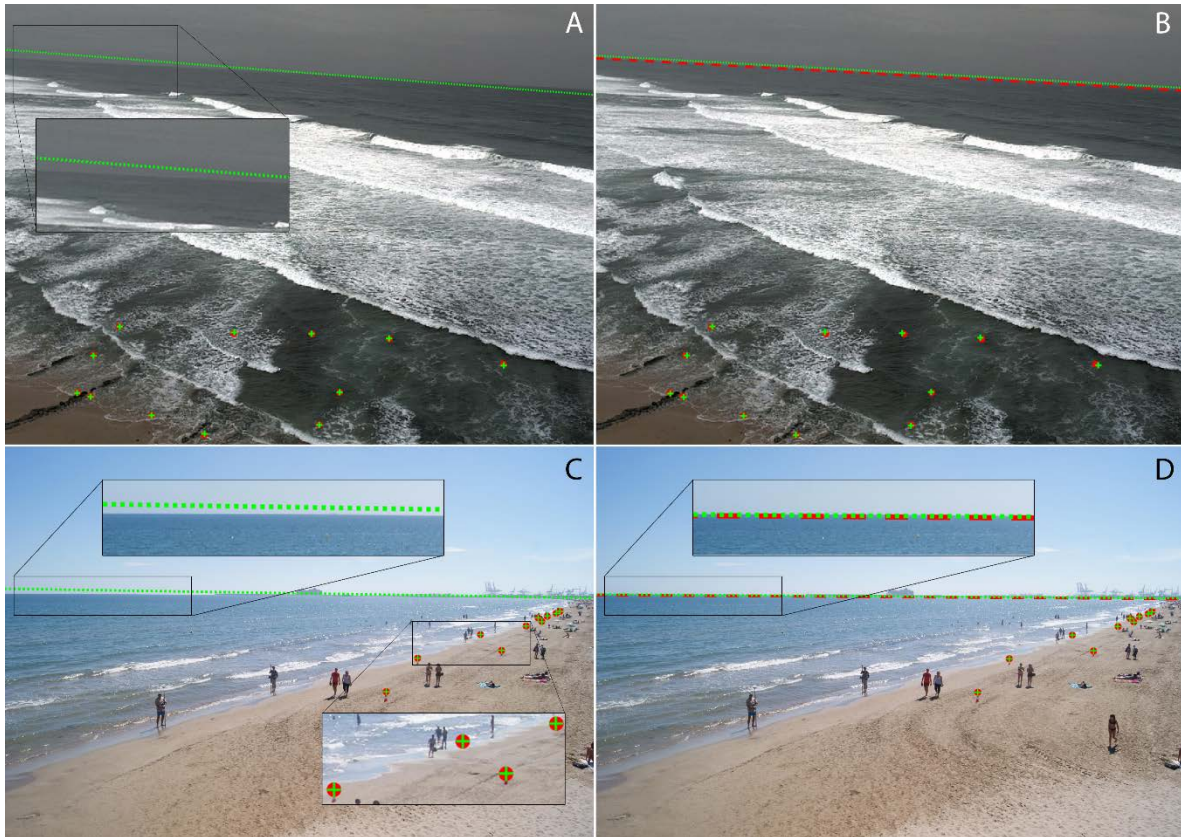
Fig. 5. Examples of the system convergence for two performances carried out at Magoito (A and B) and Patacona (C and D) beaches. The observed GCP positions and the observed horizon are shown in red respectively by points and a dashed line – adjustment input data – whereas the calculated position of these features (system solution after the iterative process) is shown in green by crosses for GCP and a dotted line for the horizon. A) and C) Wrong resulting convergence achieved without including the horizon constraint in the adjustment (the observed horizon is not involved); B) and D) Best convergence reached using the horizon as a system constraint (both with unknown IOP).

It is difficult to compute the error made in calculating the angular parameters $\{\omega, \varphi, \kappa\}$. Nevertheless, the quality of these can be analyzed through the location of the control points and the horizon line after applying step 2d) of C-Pro, as Fig. 5 shows at Magoito and Patacona beaches. Carrying out the spatial resection with unknown IOP, Figs. 5A and 5C show that in the adjustment made without including the horizon constraint, the resulting camera orientation is mistaken despite the convergence (the green line is wrongly indicating the calculated horizon direction). However, the resulting camera angles are more accurate when the horizon constraint is included in the adjustment that defines a correct horizon line. Thus, in this last case, both observed and calculated horizon lines – shown respectively in red and green in Figs. 5B and 5D – indicate an equivalent direction of the horizon.

The next assessment is made to discover in more detail the way in which the system is converging into a specific solution in accordance with to the weight assigned in the two horizon equations of (3). The system is then solved several times for the same example – using the same photo and its associated GCP file – and adding weight each time to the horizon equations. The usefulness of the horizon constraint will be studied in Fig. 6 by analyzing the CPE of seven photos from Patacona beach. These seven cases show, even when horizon equations are not intervening (cases with a weight equal to zero), that the system always converges in a solution for the spatial resection even when the IOP are unknown. However, the achieved CPE decreases as

the horizon equations gain more weight (see Fig. 6). This is evidenced in those cases where the adjustment has been carried out with nine free parameters (examples with unknown IOP) and because the horizon constraint has not considered that the CPE are higher than 2 m. Additionally, in these cases it is interesting to note that the minor CPE occurs for horizon weights equal to 10^2 and 10^4. This improvement in the accuracy of the camera coordinates happens while the solution for the rest of the parameters (three camera angles and IOP) worsens. The system is less stable when the IOP are unknown and cannot find a valid solution for the entire set of parameters until the weight of the horizon increases.

The CPE remains unchangeable from a weight equal to 10^{12} for both horizon equations although it is almost stabilized from using a weight equal to 10^8. Thus, horizon equations will be added in the adjustment in step 2c) of C-Pro with a designated weight equal to 10^{12} and can be modified by the user.
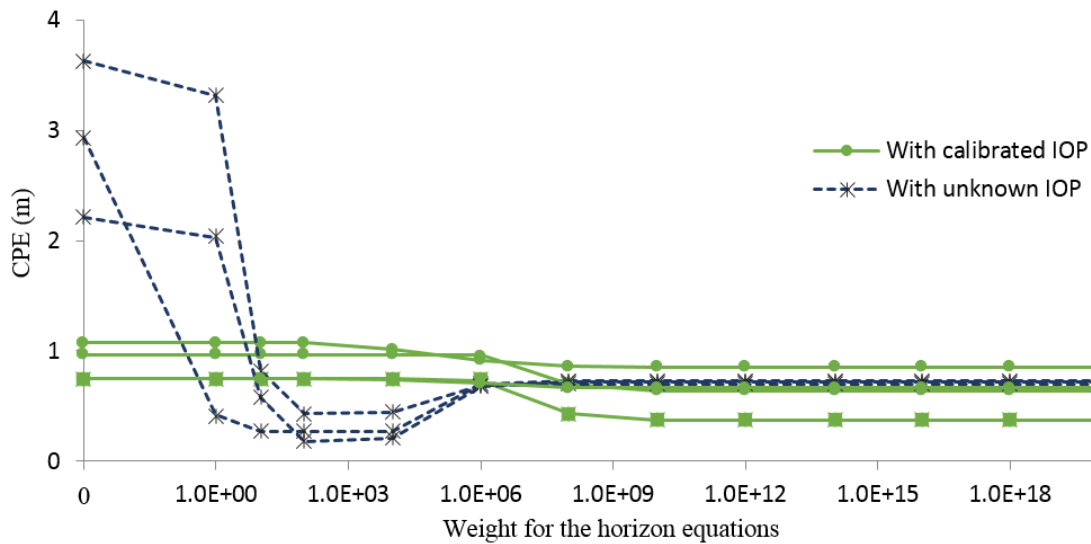
Fig. 6. CPE (m) obtained with C-Pro in seven different photos from Patacona beach are consistent with the assigned weight value in the two horizon equations of (3). The elevation of the camera ranges between 4.69 m and 6.81 m.

3.3. Usefulness and differences between both horizon approximations

After checking the improvement achieved by introducing the horizon constraint in the spatial resection process, it is important to establish the quality of the two horizon approaches developed in this paper. Therefore, this section analyzes their potential and limitations when these geometric equations are constraining the fitting. With regards to the definition of the horizon equations, it is expected that the correct choice of one or another approach (with two or three points) was conditioned by the percentage of horizon that appears in the photo.

The acquisition of a large set of photos for two days at El Saler beach with different percentages of horizon contained on the photographs enables us to analyze the error achieved in the spatial resection solution depending on the horizon approximation used during the process. Assessments are made by following the methodological protocol considering the IOP as unknown. Summarizing the results (see Table 2), we observe unacceptable results regardless of the camera location, and regardless of whether the camera is pointing north (CNi) or south (CSi), when the horizon constraint is not considered because the fitting does not converge (or it converges on a wrong solution).

		Without horizon constraint	With horizon constraint		% horizon seen in the photo
			two points	three points	
25 May 2016	CN1	Without convergence	0.139	0.930	51.5
	CN2	15.029	1.478	1.359	100
	CN3	Without convergence	0.956	0.826	100
	CN4	6.854	0.635	0.393	90
	CS1	15.118	0.568	1.105	61.7
	CS2	3.839	0.976	0.896	100
	CS3	2.769	2.041	1.891	89
17 June 2016	CN1	Without convergence	0.114	1.460	51.5
	CN2	17.516	2.164	2.010	100
	CN3	Without convergence	1.092	0.872	100
	CN4	6.332	0.586	0.491	90
	CS1	12.989	1.472	2.198	61.7
	CS2	1.649	0.729	0.669	100
	CS3	12.05	1.616	1.077	89
Average		9.414	1.227	1.048	

560 Table 2. CPE (m) obtained without known IOP in various cases, with or without the horizon constraint at El
561 Saler beach. Horizon is approximated using two or three image points, respectively. Last column shows the
562 percentage of the horizon visible in the image and not hidden behind other elements. CNi and CSi indicate
563 respectively north and south – depending on where the camera points.

565 The errors in the camera repositioning for both days indicate that the horizon approach obtained by three
566 points leads to better results unless the horizon covers less than 62% of the photo area – as occurred in both
567 CN1 and CS1 photos where the horizon remain partially hidden by the Port of Valencia (see example in Fig.
568 2). Predictably, the horizon approach calculated by three points is more realistic, but is also more sensitive
569 and requires a significant distance between points to define a descriptive horizon circumference. In general,
570 when the horizon just appears in a proportion less than 75% of the photo, the approximation must be defined
571 by two points.

573 Representing the results graphically in Fig. 7, the pattern followed by the CPE repeats for both studied days.
574 The most rigorous solutions for the spatial resection process are achieved by using the horizon approximation
575 with three points, with smaller errors in the camera positioning until the percentage of the apparent horizon in
576 the photo exceeds a specific limit as occurs in CN1 and CS1 (small circles). It is in these cases when the
577 pattern of error reverses and the errors caused by using the approximation with two points becomes smaller.
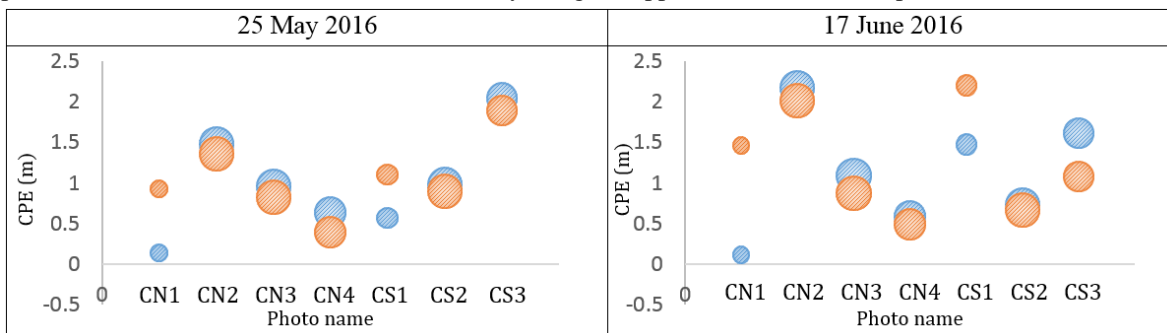
578
579 Fig. 7. CPE (m) obtained by using the two horizon approximations in seven photographs from El Saler beach

580 and for two different days. Blue represents the results achieved by using the two point horizon approximation
581 (case a), and red indicates those obtained by the horizon approximation defined with three points (case b). The
582 circle size increases with the proportion of horizon visible in the photo.
583
584 Moreover, by calculating the differences between the CPE obtained by using both horizon approximations we
585 realize that the negative values correspond with those cases where the horizon is scarce in the photo. A clear
586 relation exists when comparing these differences against the percentage of horizon, reaching $R^2 = 79.72\%$
587 in the linear fit (Fig. 8) and $R^2 = 90.25\%$ by fitting a second order polynomial model.
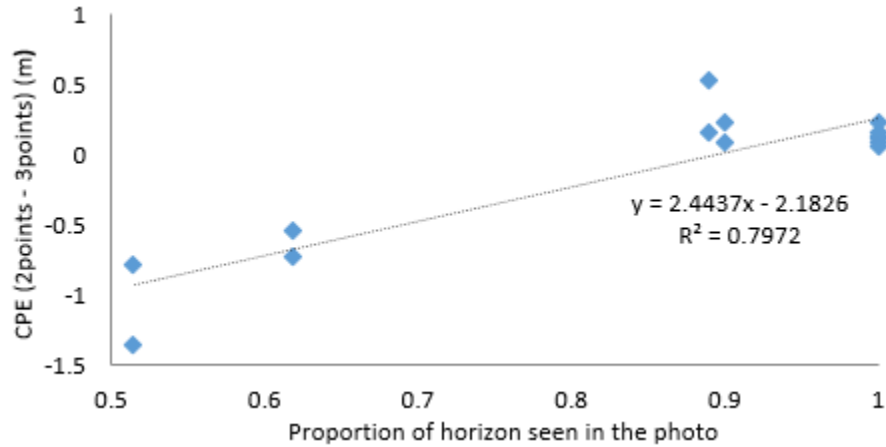
588
589 Fig. 8. CPE of Fig. 7 as a function of the proportion of horizon seen in the photo.
590
591 With regards to the conclusions obtained through these experiments, it is easy to know why at Magoito beach
592 (where the photos contain a full view of the horizon) the approximation achieved by three points led to
593 slightly better results as seen in Table 1. Two-point horizon approximation was used at Patacona beach
594 because the horizon appeared in less than half of the image.
595
596 **3.4. Analysis of errors after the image rectification process**
597
598 The final accuracy of the system depends on many factors. This subsection is focused on managing the errors
599 related to the image rectification process through the implementation of a rigorous algorithm (after step 3). To
600 assess the overall positional accuracy for the rectified images in the three study areas, several terrain points –
601 those not used to solve the geometry and termed checkpoints – were computed solving (10) and comparing
602 their projected computed coordinates (X, Y) against GPS coordinates after step 3 of C-Pro. Formula (12)
603 calculates this error (which is composed by both cross-shore and longshore components).

604
$$Positional\ error = \sqrt{(X_{GPS} - X)^2 + (Y_{GPS} - Y)^2} \qquad (12)$$

605 Moreover, regarding the camera position and the focal length, the pixel footprint will be calculated to obtain
606 the dimension of each pixel in the terrain space.
607
608 The first analysis was made at Magoito beach using the orientation parameters achieved in the best case with
609 calibrated IOP and the horizon constraint approximated by three points (see Table 1). Despite the 0.97 m of
610 error recorded in the camera repositioning, the checkpoints – 65 to 98 m distant from the camera – are
611 positioned with an average accuracy of 0.201 m. Moreover, Fig. 9 shows a slight relation between each
612 positional error and the distance to the camera because of the perpendicular GCPs distribution relative to the
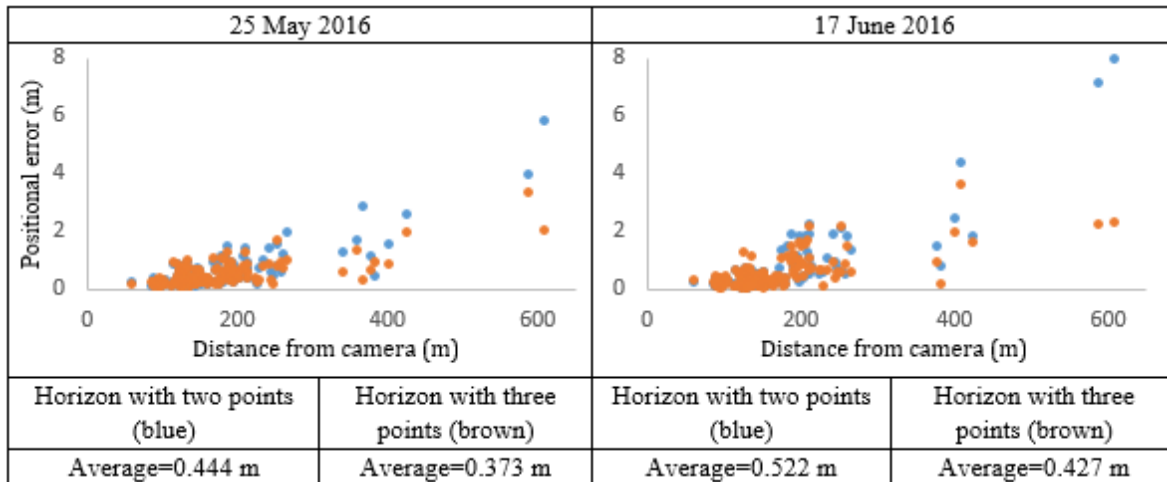613 camera position (remember Fig. 1 in the data section).
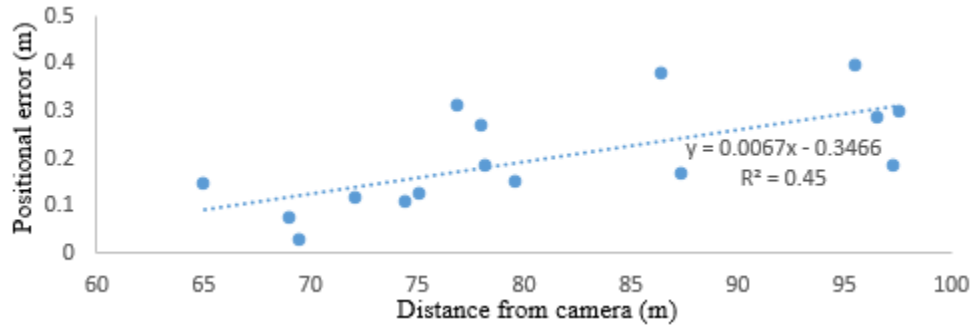
Fig. 9. Scatter plot that relates the behavior of the positional errors in the checkpoints at Magoito beach relative to their distance from the camera.

The error is dominated by the cross-shore component through the target area and, as expected, is closely related with a pixel footprint smaller than 0.5 m.

The second experiment at El Saler beach (see Table 2) also includes a study of projected errors in the checkpoints using the horizon approximation in the spatial resection system with unknown IOP. It is important to remember that the photos will be different every day because we are not working with a fixed camera. As a result, the GCPs image coordinates, the resulting spatial resection, and the final image rectification, will change.

Fig. 10 shows that differences between averages of positional errors using each of the two horizon approximations are smaller than 0.1 m. Again, the results indicate that in most cases, those errors are lower when the horizon constraint is obtained following the approximation with three points. If the horizon visibility requirements are overtaken, we should then follow the methodology where the horizon curve is approximated as the tangent line to a circumference. Furthermore, Fig. 10 proves an increasing trend of the positional errors with respect to the camera distance. However, up to a distance of 200 m, errors in the checkpoints respond to a similar behavior for both horizon approximations. Considering only the points with distances to the camera of less than 200 m, the average positional error for the 25 May is equal to 0.286 m using the horizon approximation with two points and 0.283 m using the three-point approximation. For the 17 June, both results are equal to 0.275 m and 0.273 m, respectively. However, from 200 m to 610 m, the differences in the positional errors obtained for each horizon approach become more apparent. The averaged results verify the success of the horizon approximation with three points with values equal to 0.793 m and 1.140 m, respectively for 25 May and 17 June, meanwhile using only two points, those values reach, in the same checkpoints, 1.170 m and 1.670 m respectively.

	25 May 2016		17 June 2016	
	Horizon with two points (blue)	Horizon with three points (brown)	Horizon with two points (blue)	Horizon with three points (brown)
	Average=0.444 m	Average=0.373 m	Average=0.522 m	Average=0.427 m

Fig. 10. Variation of the positional accuracy (m) with distance from the camera at El Saler beach depending on the horizon approximations (two or three points) used for spatial resection. The rectification process has been made for the seven different photos in each of the two days described in Table 2 considering unknown IOP.

Furthermore, it is important to establish the differences in magnitude between both cross-shore and longshore error components (see Fig. 11) depending on the phenomenon analyzed. For instance, when the photos are used to extract longitudinal coastal features such as the water/land border, the positional accuracy will be dominated by the cross-shore component. Comparing a surveyed RTK-GPS shoreline and another obtained from the rectified images as illustrated in Fig. 12 – projected on the corresponding sea level elevation – the root mean square error (RMSE) was 1.482 m and 1.645 m for 25 May and 17 June respectively. These encouraging results are in line with other similar works such as Taborda and Silva (2012) where the swash line position is rectified with an RMSE of 1.4 m, and Bracs et al. (2015) where the surfcam-derived shorelines are calibrated against Argus shorelines with an error less than 1.9 m.
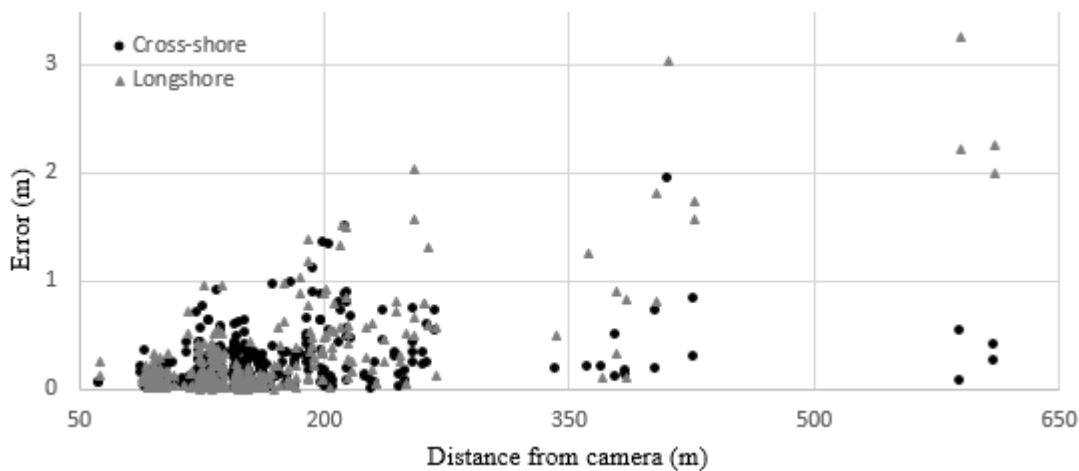

Fig. 11. Cross-shore and longshore errors for data used in Fig. 10 at El Saler beach. The errors are obtained when carrying out the best spatial resection solution obtained in each case.

664   Fig. 12. Projection map with the rectified photos of 25 May 2016 for El Saler beach shown over an
665   orthophoto taken from 2010 PNOA sources. The four different shots are obtained from the CN position (north
666   camera). It is important to know that the projection is made at 0.129 m above mean sea level – as near in time
667   with the photos as possible – whereas the RTK-GPS shoreline (green line) has an average elevation of 0.11 m.
668   Grid coordinates: GCS_ETRS89 UTM.
669
670   For the last analysis, at Patacona beach, the evaluation of the image rectification process was made by
671   checking the coordinates of several measured terrain points to thoroughly analyze the longitudinal component
672   of error (longshore positional accuracy). The acquisition process measuring points by progressively moving
673   the GPS trackers towards the shoreline while each photo was taken is explained in the data section.
674   Furthermore, this data is used to continue with the analysis of errors depending on the spatial resection
675   adjustment carried out (cases s1 to s4) and which is expected to be in line with the CPE previously shown in
676   Table 1.
677
678   When the adjustment was computed by just six free parameters (data pointed in Fig. 11), the average error
679   was 2.48 m or 4.29 m depending on whether the horizon constraint was considered (s2) or not (s1). The
680   horizon approximation has been computed with only two points as in Fig. 13. Moreover, when the IOP are
681   unknown (data dashed in Fig. 11), the errors were worse and reached 3.91 m with horizon constraint and 5.69
682   m without. These higher magnitudes of error, compared with those obtained in the above two beaches, are
683   consequences of the low-elevation cameras (only 4.7 m to 6.8 m high) and the pixel rectification error
684   associated with obliquity. This fact greatly complicates the detection of the checkpoints in the photography
685   with clarity being rapidly lost with distance. These difficulties are also linked with the limitations of the
686   camera optics. An initial study analyzing both cross-shore and longshore errors (see Fig. 13) indicates that
687   some problems in the manual detection of the checkpoints are expected – with errors in their real positions
688   because of visual obstructions such as beach berms. This fact is very influential in longshore error as it is
689   more sensitive to the distance from the camera and where a single pixel at 200 m distance means 1 m of error
690   in the geographic space. However, the valid magnitudes for the cross-shore components indicate the ability
691   and solvency of the methodology for detecting coastal indicators.
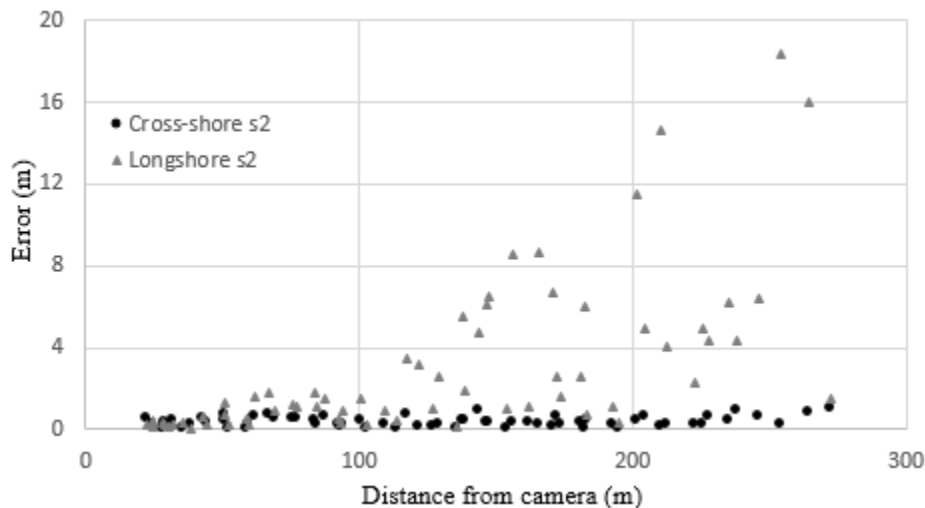
692
693   Fig. 13. Cross-shore and longshore positional accuracies after the rectification procedure (calibrated IOP &
694   with HC) obtained for some GPS points measured on the shoreline at Patacona beach.
695
696   The next analysis focuses just on those points located less than 200 m from the camera, discarding the others
697   as reliable for computing the overall error. By averaging these selected points, we obtain positional accuracies
698   reaching 1.68 m when the image rectification is computed following s2, 2.86 m with s1, 2.91 m with s4, and
699   4.56 m in the worst case through s3.
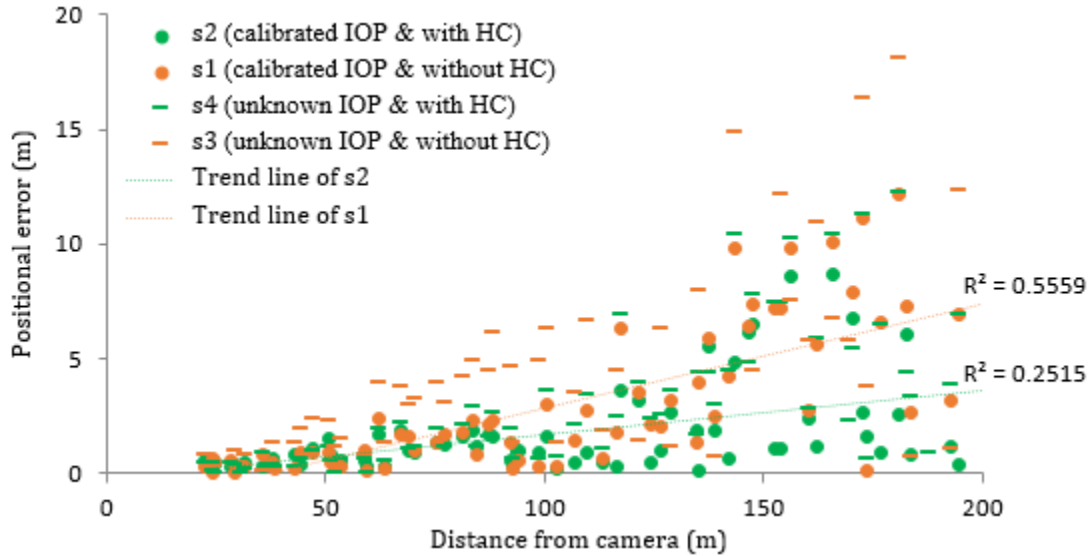
Fig. 14. Variation of the positional error with distance from the camera depending on the methodological process carried out. We detected points in 25 photos at Patacona beach (spatial resection was already analyzed in Fig. 4). Remember that the photos were taken with low-elevation cameras that range from 4.7 m to 6.8 m high.

Results verify that despite not knowing the IOP, similar averaged errors obtained for s1 and s4 mean that the use of the horizon constraint provides solutions as valid as those obtained when the initial parameters are calibrated. Moreover, we realize in Fig. 14 that positional errors have a strong dependence on camera distance. Longitudinal errors grow excessively when the horizon constraint is not included ($R^2 = 55.59\%$) whereas its use slows this fact ($R^2 = 25.15\%$) by leading the rectified image to a proper alignment.

4.   Discussion and conclusions

This paper has described a new coastal projector monitoring system called C-Pro which uses terrestrial photogrammetry to project a photograph in a georeferenced plane. The main novelty, compared with other methods previously described in the literature, lies in the definition of a mathematical formulation that incorporates information provided by the location of the horizon curve in the image. For this, the roll and pitch rotation angles have been computed from an approximation of the horizon curve to define the transformation from image vectors to terrain vectors. This describes the change between coordinate reference systems: from object space to image space. The relationship between these rotation angles and the EOP of the camera leads to the horizon equations. Thus, an initial solution of these angular parameters can be obtained from horizon equations, which are also used in the repositioning process of the camera as constraints providing two degrees of freedom. Oreifej et al., (2011) already exploited the horizon line in terms of providing a unique unambiguous solution for recovering the UAV camera motion.

C-Pro has been applied to three different coastal areas using two cameras located at several elevations ranging from 4.7 m (Patacona beach) to 43 m (El Saler beach). Results have shown the improvement that occurs in estimating the camera positioning when adding the horizon constraints, especially in the case of using cameras with unknown IOP. Sometimes, the iterative least squares fitting – over the linearized collinearity equations – does not converge unless the horizon constraints are used. In other cases, although the system converges, the achieved solution is not useful and the horizon equations help reduce errors in camera positioning and angular parameters $\{\omega,\varphi,\kappa\}$. The quality of the spatial resection has also been analyzed by coloring the resulting image location of the control points and the horizon line using the calculated parameters after each iteration. Errors are smaller when weights assigned to horizon constraints in that refinement process are much higher than those given in equations associated with GCPs.

Image coordinates of three points are used to approximate the horizon curve. However, results have shown that a horizon approach with two points is more accurate in situations in which only a part of the horizon is seen in the image. The horizon approach calculated by three points is more realistic but is more sensitive and requires a significant distance between points to define a descriptive horizon circumference.

Some terrain points with known GPS coordinates, which have not been involved in the setting as GCPs, were also computed with C-Pro to assess the overall positional accuracy over the rectified images in the three coastal areas. At Magoito beach, the checkpoints situated less than 65 m from the camera were positioned with an averaged accuracy of 0.2007 m. Moreover, errors were less than 0.5 m for points located within 100 m of the camera. Those errors of projection were obtained after placing the camera with an elevation of 35.6 m, using C-Pro with calibrated IOP, and approximating the horizon constraint with three points.

Errors at checkpoints increase slightly when the IOP are unknown as is assessed in El Saler beach where the camera was located at the top of a building 43 m high. However, acceptable results are obtained by considering the horizon approximation in the spatial resection system, computed following the approximation with three points. Those results have been obtained with a non-fixed camera taking 14 photos in two days. Consequently, as the GCPs image coordinates will change, the resulting spatial resection will also differ for every photo. Considering the checkpoints whose distances to the camera were less than 200 m, the average error was equal to 0.283 m on the first day and 0.273 m on the second day.

At Patacona beach, the camera is located at an elevation ranging between 4.7 and 6.8 m. In this case, we analyze the longshore error through an experiment measuring shoreline points until a distance of less than 200 m from the camera is found that is considered as reliable for computing that error. Positional accuracies reached an average positional error equal to 1.68 m when the image rectification was computed using calibrated IOP and 2.91 m when considering unknown IOP. The horizon approximation with two points was used in these cases because the horizon appeared in less than half of the image. Thus, the use of the horizon constraint has enabled us to obtain valid solutions even in cases when it is not possible to obtain the IOP by camera calibration (or other complicated photogrammetric conditions such as low camera elevations were present).

The methodology developed in this work enables accurately projecting a coastal photograph – or any element detected in it – on a georeferenced plane, even if the photo was taken by a camera with unknown IOP and located at a less than 7 m high. Encouraging results (similar to those obtained by Taborda and Silva, 2012) which are able to define the shoreline with an RMSE of less than 1.5 m. Its implementation in C-Pro, through formulas detailed in this paper, makes it a robust and low-cost tool that can work with any photograph taken by a conventional camera of a coastal segment with the horizon included. In this paper, the horizon points have been marked manually but future works applying C-Pro will use techniques that automatically track the horizon (Bracs et al., 2015; Oreifej et al., 2011).

The application of C-Pro will produce valuable scientific information from numerous cameras and video cameras located along coastlines worldwide. Although in principle these recreational cameras were set for other non-metric goals, they can now also be useful for measuring beach indicators for better planning and managing coastal resources.

Acknowledgements

Appendix A: Horizon constraint

791
792 The methodology of terrestrial photogrammetry described in this paper is designed for use in coastal imaging
793 systems where the horizon is an element of the photo (meaning the separation between sea and sky).
794 Appendix A describes some mathematical tools that take advantage of the information provided by the
795 horizon line and are useful for the new coastal projector monitoring system (C-Pro), explained in Section 2.
796
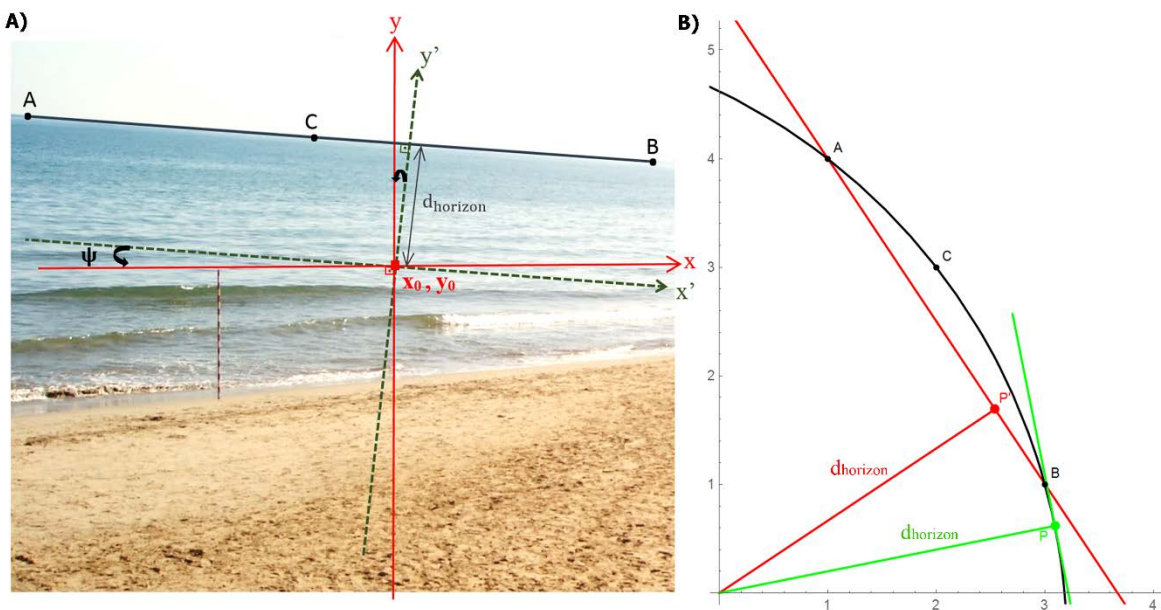797 **A.1. Image orientation using the horizon**
798
799 The calculation of the image orientation with respect to the object space is made through three rotations and
800 three corresponding angles that transform image data into real-world coordinates: $\omega \in [-\pi, \pi], \varphi \in$
801 $[-\pi/2, \pi/2], \kappa \in [-\pi, \pi]$. $R_{\kappa\varphi\omega}$ consists of the product between an initial rotation matrix in the Z axis,
802 later in Y axis, and finally in the X axis. Thus, (X, Y, Z) coordinates of a point in the object reference system
803 focused on the main point of the image can be calculated by knowing its associated coordinates (x, y, z) in the
804 image reference system.
805
806 In the following paragraphs the (x, y, z) coordinates in the image space are referred to as the principal point
807 $o = (x_0, y_0)$ and to simplify formulas in this section, its coordinates are assumed as zero $o = (0,0)$. Both the
808 object coordinates and the image coordinates – originally defined from the upper left corner of the image –
809 are translated by establishing its origin in the principal point. However, there are other rotational angles
810 relating both image and object coordinates such as described by Dai et al., 2011 and Rodríguez et al., 2008.
811 We are going to use several of these ideas to define the equations of change between reference systems
812 through new angles.
813
814 The definition of these angles is based on the approximation of the Earth's curved horizon as a straight line in
815 the image plane. Two alternatives for the determination of that straight line are proposed in this paper by
816 marking two vanishing points in the image that are as distant as possible; A = (x_a, y_a), B = (x_b, y_b), and fulfil
817 that $x_a < x_b$. In this paper, the horizon points have been marked manually to ensure that they do not become an
818 added source of error in the methodological assessment.

819
820 Fig. A.1. Image orientation: A) changing the coordinate system in the image space where the angle ψ is
821 defined; and B) representation of both horizon approximations: shown as a red line following case a) and in
822 green for case b).

823

824   **Case a)** (two points) The horizon curve is approximated through the line joining both A and B points (colored
825   red in Fig. A.1B).

826

827   **Case b)** (three points) If A and B points are far enough apart, it is possible to find a third point $C = (x_c, y_c)$.
828   These three points define a circumference and we compute P as the point where the minimum distance is
829   reached between the circumference and the principal point of the image plane. The tangent line to the
830   circumference at such point P then approximates the real curved horizon (shown in green in Fig. A.1B).

831

832   Note that the horizon approximation with three points is the most realistic. However, it is very sensitive and
833   strongly dependent on the horizon extension seen in the image. If the three points responsible for forming the
834   circumference are too close to each other due to the reduced horizon extension, it will not be reliable and we
835   should proceed using the methodology with two points described in case a). In the results section, the
836   influence of this horizon requirement is analyzed.

837

838   Therefore, considering some of the above procedures, the horizon curve is finally approximated through a
839   straight line. Assuring the consistency of a semi-automatic process, we need to have control over the correct
840   order in the manual input of the image coordinates verifying that $x_a < x_c < x_b$ (see Fig. A.1A). Moreover, these
841   should verify that in the ABC triangle, the C internal angle ranges $]0, \pi[$.

842

843   To define the new rotation angles from the calculated horizon line –widely known as roll and pitch angles
844   (Oreifej et al., 2011) – it must be remembered that such a horizon line is parallel to both the object plane
845   (defined by the XY-plane of the object space) and the image plane where it is placed. Therefore, we can use
846   the horizon line as the rotational axis of the image plane for image orientation (Rodríguez et al., 2008). Thus,
847   the (x, y, z)-image coordinate system rotates into the (X,Y,Z)-object coordinate system through the three
848   following sequential steps.

849

850   **Step 1:** $\vec{v}_{AB}$ is considered as the perpendicular vector to the straight line connecting A and B points in which
851   the second coordinate is positive. We then compute ψ as the angle formed between such a vector and the
852   vertical vector (0,1) – that is the complementary one of the roll angle used in Cornall and Egan (2004). The
853   definition of ψ will change in accordance with the horizon approximation:

854

855   Case a) (two points) Being the horizon the straight line defined by the points A and B then $\vec{v}_{AB} =$
856    $(y_a - y_b, x_b - x_a)$, and the angle ψ may be defined as:

857

858            $$\psi = \arctan((y_a - y_b)/(x_b - x_a)) \in \,]-\pi/2, \pi/2[, \qquad \text{being } x_a < x_b \qquad (A.1)$$

859

860   Case b) (three points) approaching the horizon through the tangent line to the circumference passing
861   through the points A, B and C then $\vec{v}_{AB}$ is the direction of the line which connects the center of this
862   circumference with the principal point $o = (0,0)$ of the image plane. Consequently, $\vec{v}_{AB} = (c_x, c_y)$ if $c_y > 0$
863   or $\vec{v}_{AB} = (-c_x, -c_y)$ if $c_y < 0$, where (c_x, c_y) are the coordinates of the circumference center in the image
864   plane with respect to the principal point. This center is previously obtained as the intersection point between
865   the line perpendicular to the segment AC that passes through its midpoint and the line perpendicular to the
866   segment CB through its midpoint. Finally, the angle ψ is defined as:

867

868            $$\psi = \arctan(-c_x/-c_y) = \arctan(c_x/c_y) \in \,]-\pi/2, \pi/2[, if \; cy \neq 0 \qquad (A.2)$$

869

870   In formula (A.2) it is assumed that the principal point is closer to the horizon than the ABC circumference
871   center. Moreover, ψ has the following definition in the cases in which c_y could be equal to 0:

872
$$\begin{cases} if \; c_y = 0 \; and \; c_x < 0 \rightarrow \psi = \pi/2 \\ if \; c_y = 0 \; and \; c_x > 0 \rightarrow \psi = -\pi/2 \end{cases} \qquad (A.3)$$

873   The xyz-system rotates a clockwise angle $(-\psi)$ in the plane z=0, so the new x' axis will be parallel to the
874   horizon line (see Fig. A.1A). The coordinates of any point in the xyz-system are related with the x'y'z'-
875   system by:

876
$$\begin{pmatrix} x \\ y \\ z \end{pmatrix} = \begin{pmatrix} \cos(-\psi) & -\sin(-\psi) & 0 \\ \sin(-\psi) & \cos(-\psi) & 0 \\ 0 & 0 & 1 \end{pmatrix} \begin{pmatrix} x' \\ y' \\ z' \end{pmatrix} = \begin{pmatrix} \cos(\psi) & \sin(\psi) & 0 \\ -\sin(\psi) & \cos(\psi) & 0 \\ 0 & 0 & 1 \end{pmatrix} \begin{pmatrix} x' \\ y' \\ z' \end{pmatrix} = R_\psi \begin{pmatrix} x' \\ y' \\ z' \end{pmatrix} \quad (A.4)$$

877
878   In this first step the rotation angle $(-\psi)$ does not consider the position of the horizon line with respect to the
879   x-axis. Formulas (A.1), (A.2) and (A.3) only take into account the orientation of the vector perpendicular to
880   the horizon line with respect to the y-vector direction. For this reason, in the next step we will consider the
881    $d_{horizon}$ sign, which represents the minimal distance in the image plane from the principal point to the
882   approached horizon line. Thus, $d_{horizon}$ could have a negative sign if the closest point of the horizon line to the
883   principal point has a negative y-coordinate. Again, as expected, calculation of $d_{horizon}$ depends on the horizon
884   approximation as follows:
885
886   Case a) (two points) Following this first approximation, the minimal distance between the principal point and
887   the horizon line is:

888
$$d_{horizon} = \frac{y_a x_b - y_b x_a}{\sqrt{(x_b - x_a)^2 + (y_b - y_a)^2}} \qquad (A.5)$$

889
890   Case b) (three points) However, in this other case, the minimal distance will be calculated as: $|d_{horizon}| =$
891    $r - \sqrt{c_x^2 + c_y^2}$, being r the radius of the ABC horizon circumference. It should be remembered that given the
892   characteristics of the horizon, we can assume – without loss of generality – that the principal point is within
893   the circumference. Therefore, the sign of $d_{horizon}$ is calculated as follows:

894
$$\begin{cases} d_{horizon} = r - \sqrt{c_x^2 + c_y^2} > 0 \; if \; c_y < 0 \\ d_{horizon} = \sqrt{c_x^2 + c_y^2} - r < 0 \; if \; c_y > 0 \end{cases} \qquad (A.6)$$

895
896   In cases where $c_y = 0$ then:

897
$$\begin{cases} if \; c_y = 0 \; and \; c_x < 0 \rightarrow d_{horizon} = r - |c_x| > 0 \\ if \; c_y = 0 \; and \; c_x > 0 \rightarrow d_{horizon} = |c_x| - r < 0 \end{cases} \qquad (A.7)$$

898
899   Moreover, both procedures enable calculating the coordinates of the horizon point P (x_P, y_P) in the image
900   plane centered at principal point $o = (0,0)$ as:

901
$$\begin{cases} x_P = d_{horizon} * \sin(\psi) \\ y_P = d_{horizon} * \cos(\psi) \end{cases} \qquad (A.8)$$

902
903   It is necessary to consider in (A.8) the appropriate sign of $d_{horizon}$ as explained above. The observed horizon
904   line could then be indicated in the photos as Fig. A.1A shows.

905
906 **Step 2:** Once the x' axis is positioned parallel to the horizon line, the image plane must be oriented parallel to
907 the object plane by means of another rotation angle $(-\xi)$ – that is the complementary one of the pitch angle
908 defined in Schwendeman and Thomson (2015). The x'y'z'-coordinate system rotates a clockwise angle $(-\xi)$
909 to generate an x''y''z''-coordinate system, being x''=x' and z''=Z (the elevation coordinate). Thus, in this
910 step the image orients around the x' axis, keeping this parallel to the horizon line and positioning the y'-axis
911 on a plane which passes through the principal point and is parallel to the object plane (XY) (see Fig. A.2). In
912 this way, $(-\xi)$ coincides with the angle formed between y*' axis (whose origin is C_c and is parallel to y') and a
913 plane parallel to the terrain pointing to infinity (y*'').
914
915 We consider the vector $\vec{v}$ perpendicular to the object plane whose origin is the optical center of the camera.
916 The ξ angle (represented in Fig. A.2) then coincides with the angle formed between such vector $\vec{v}$ and the
917 vector perpendicular to the y'-axis that goes from the camera's centre C_c to the principal point o.
918
919 In the triangle formed by C_c, o and P (the point where the minimum distance between the principal point and
920 the horizon line is reached), the angle $\widehat{C_c}$ can be calculated as:
921

922
$$\widehat{C_c} = arctan(d_{horizon}/f) \in \left]-\frac{\pi}{2}, \frac{\pi}{2}\right[\qquad (A.9)$$

923
924 being f the positive value of the camera focal length which coincides with the distance between C_c and o. We
925 note that the meaning of that angle is from the vector $\overrightarrow{C_c\,o}$ to $\overrightarrow{C_c\,P}$ and its sign coincides with $d_{horizon}$,
926 distance as defined by formulas (A.5)-(A.7) and which can be positive or negative.
927
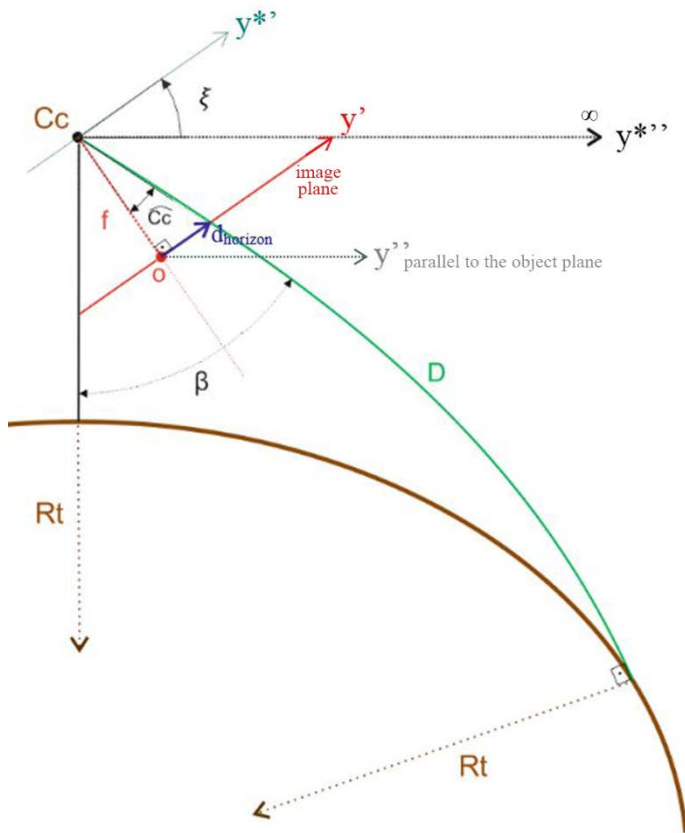
928
929 Fig. A.2. Spatial orientation of the image with the graphical definition of angle ξ.

930

931 Naturally, the scope of our vision to the horizon will depend on the height (Z_{C_C}) at which the observer is
932 located, as well as the existent geographic features in front of our view. It is known that the field of view of
933 the ground surface extends from the observer's feet to the horizon (Ooi et al., 2001) establishing a
934 trigonometric relationship where an object at infinity is seen as uppermost. Knowing the elevation of the
935 camera $Z_{C_C} > 0$, and being R_t the approximate radius of the Earth (6371 Km), we can then compute an
936 approximation to the geographical distance D between the observer and the horizon by means of the formula:

937

938
$$D = +\sqrt{(Z_{C_C} + R_t)^2 - R_t^2} > 0 \quad (A.10)$$

939

940 When sitting on the beach, facing the sea, and looking one-meter above the water, the horizon will be
941 distinguished within D=3.57 km. However, this observed distance will increase - although disproportionally –
942 as height increases.

943

944 The next step is to compute the angle β between $\vec{v}$ vector and the line between the observer and the horizon.
945 To achieve this we take into account the refraction and terrestrial sphericity correction (1 mm of error in 100
946 m of distance). However, sometimes when the observer's elevation is low, this correction becomes irrelevant.
947 The formula to calculate angle β is:

948

949
$$\beta = arcco s \left(\frac{Z_{C_C} + 0.42 * D^2/R_t}{D} \right) \in \,]0, \pi/2[\quad (A.11)$$

950 Therefore:

951
$$\xi = \beta - \widehat{C_c} = arcco s \left(\frac{Z_{C_C} + 0.42 * \frac{D^2}{R_t}}{D} \right) - arctan \left(\frac{d_{horizon}}{f} \right) \quad (A.12)$$

952

953 If $\widehat{C_c} > 0$, ξ definition must be $\xi = (\beta - \widehat{C_c}) > 0$, verifying $\xi \in \,]0, \pi[$. The extreme interval values ($\xi =$
954 $0 \, \& \, \xi = \pi$) are impossible values because the image plane would be parallel to the object plane – as happens
955 in a vertical photo – where the horizon cannot be seen.

956

957 After computing ξ by means of (A.12), the x'y'z'-system rotates the clockwise angle$(-\xi)$ about the x' axis to
958 generate an x''y''z''-coordinate system. The coordinates of any point in the x'y'z'-system can be calculated
959 from the x''y''z''-system by:

960

961
$$\begin{pmatrix} x' \\ y' \\ z' \end{pmatrix} = \begin{pmatrix} 1 & 0 & 0 \\ 0 & \cos(-\xi) & -sin(-\xi) \\ 0 & \sin(-\xi) & \cos(-\xi) \end{pmatrix} \begin{pmatrix} x'' \\ y'' \\ z'' \end{pmatrix} = \begin{pmatrix} 1 & 0 & 0 \\ 0 & \cos(\xi) & \sin(\xi) \\ 0 & -\sin(\xi) & \cos(\xi) \end{pmatrix} \begin{pmatrix} x'' \\ y'' \\ z'' \end{pmatrix} = R_\xi \begin{pmatrix} x'' \\ y'' \\ z'' \end{pmatrix} \quad (A.13)$$

962

963 **Step 3:** The third and last angle (λ) of the Euler triad is the azimuth and this positions the coordinate axis (x'',
964 y'', z'') regarding the real terrain coordinates and around the z''=Z axis.

965
$$\begin{pmatrix} x'' \\ y'' \\ z'' \end{pmatrix} = \begin{pmatrix} \cos(\lambda) & \sin(\lambda) & 0 \\ -\sin(\lambda) & \cos(\lambda) & 0 \\ 0 & 0 & 1 \end{pmatrix} \begin{pmatrix} X \\ Y \\ Z \end{pmatrix} = R_\lambda \begin{pmatrix} X \\ Y \\ Z \end{pmatrix} \quad (A.14)$$

966

967 Summarizing, these three new angles are responsible for carrying out the transformation between the image
968 vectors and the terrain vectors with an initial rotation in the image plane around the focal axis, a second
969 rotation turning on the x'' axis, and the final rotation again around the Z axis:

970
$$\begin{pmatrix} x \\ y \\ z \end{pmatrix} = R_\psi R_\xi R_\lambda \begin{pmatrix} X \\ Y \\ Z \end{pmatrix} = \begin{pmatrix} \cos(\psi) & \sin(\psi) & 0 \\ -\sin(\psi) & \cos(\psi) & 0 \\ 0 & 0 & 1 \end{pmatrix} \begin{pmatrix} 1 & 0 & 0 \\ 0 & \cos(\xi) & \sin(\xi) \\ 0 & -\sin(\xi) & \cos(\xi) \end{pmatrix} \begin{pmatrix} \cos(\lambda) & \sin(\lambda) & 0 \\ -\sin(\lambda) & \cos(\lambda) & 0 \\ 0 & 0 & 1 \end{pmatrix} \begin{pmatrix} X \\ Y \\ Z \end{pmatrix}$$

971

972 Finally, the rotation matrix can produce the change of coordinates since the image to the terrain reference
973 systems is $R_{\lambda\xi\psi} = (R_\psi R_\xi R_\lambda)^T$:

974

975
$$\begin{pmatrix} X \\ Y \\ Z \end{pmatrix} = \begin{pmatrix} \cos\lambda\, \cos\psi - \sin\lambda\, \cos\xi\, \sin\psi & -\sin\lambda\, \cos\xi\, \cos\psi - \cos\lambda\, \sin\psi & \sin\xi\, \sin\lambda \\ \sin\lambda\, \cos\psi + \cos\lambda\, \cos\xi\, \sin\psi & \cos\lambda\, \cos\xi\, \cos\psi - \sin\lambda\, \sin\psi & -\sin\xi\, \cos\lambda \\ \sin\xi\, \sin\psi & \cos\psi\, \sin\xi & \cos\xi \end{pmatrix} \begin{pmatrix} x \\ y \\ z \end{pmatrix} (A.15)$$

976

977 **A.2. Obtaining the horizon constraint**

978

979 Equating the two rotation matrices $R_{\lambda\xi\psi}$ and $R_{\kappa\varphi\omega}$ it is possible to build the following horizon constraint
980 equations. These will relate ψ and ξ angles – defined by means of (A.1) to (A.3) and (A.12) – with the three
981 known angular EOP, $\{\omega, \varphi, \kappa\}$:

982
$$\cos(\xi) = \cos(\varphi)\cos(\omega) \qquad (A.16)$$
983
$$\cos(\psi)\sin(\xi) = \cos(\varphi)\sin(\omega) \qquad (A.17)$$
984
$$\sin(\psi)\sin(\xi) = -\sin(\varphi) \qquad (A.18)$$

985

986 Because $\psi \in [-\pi/2, \pi/2]$, $\xi \in\,]0, \pi[$ and $\varphi \in [-\pi/2, \pi/2]$ then $\cos(\psi) \geq 0$, $\sin(\xi) > 0$ and $\cos(\varphi) \geq 0$.
987 Consequently, by using equation (A.17) we may conclude that $\sin(\omega) \geq 0$, and so $\omega \in [0, \pi]$. When $\psi \in\,] -$
988 $\pi/2, \pi/2[$ then $\cos(\psi) > 0$ and it is possible to confirm that $\varphi \in\,] - \pi/2, \pi/2[$ and $\omega \in\,]0, \pi[$. Moreover, we
989 notice that $\psi = \pm\pi/2$ only in cases when we apply equation (A.3) for computing ψ. In those cases:

990
$$\psi = \frac{\pi}{2} \rightarrow \begin{cases} \varphi = -\xi, & \omega = 0 & if\ \xi \in\,]0, \frac{\pi}{2}[\\ \varphi = \xi - \pi, & \omega = \pi & if\ \xi \in\,]\frac{\pi}{2}, \pi[\\ \varphi = -\frac{\pi}{2}, \omega\ unknown & & if\ \xi = \frac{\pi}{2} \end{cases} \quad and\ \psi = \frac{-\pi}{2} \rightarrow \begin{cases} \varphi = \xi, & \omega = 0 & if\ \xi \in\,]0, \frac{\pi}{2}[\\ \varphi = \xi - \frac{\pi}{2}, & \omega = \pi & if\ \xi \in\,]\frac{\pi}{2}, \pi[\\ \varphi = \frac{\pi}{2}, \omega\ unknown & & if\ \xi = \frac{\pi}{2} \end{cases}$$

991

992 Thus, without loss of generality, in the following steps we will assume that $\psi \in\,] - \pi/2, \pi/2[$, $\varphi \in\,] -$
993 $\pi/2, \pi/2[$ and $\omega \in\,]0, \pi[$. Equation (A.18) tells us that $\sin(\psi)$ and $\sin(\varphi)$ have different signs and so:

994
$$\left. \begin{array}{ll} \varphi \in\,]0, \pi/2[, & If\ \psi \in\,] - \pi/2, 0[\\ \varphi \in\,] - \pi/2, 0[, & If\ \psi \in\,]0, \pi/2[\\ \varphi = 0, & If\ \psi = 0 \end{array} \right\} \qquad (A.19)$$

995

996 However, we can distinguish three different situations in accordance with equation (A.16):

997

998
$$\left. \begin{array}{ll} \omega \in\,]0, \pi/2[, & If\ \xi \in\,]0, \pi/2[\\ \omega \in\,]\pi/2, \pi[, & If\ \xi \in\,]\pi/2, \pi[\\ \omega = \pi/2, & If\ \xi = \pi/2 \end{array} \right\} \qquad (A.20)$$

999

1000 Joining (A.17) and (A.18) and considering that $\varphi \in\,] - \pi/2, \pi/2[$ and $\omega \in\,]0, \pi[$, equations (A.16)-(A.18) lead
1001 to the following equation system:

1002

$$\left.\begin{array}{l}\cos(\xi) = \cos(\varphi)\ \cos(\omega)\\[4pt]\tan(\psi) = \dfrac{-\sin(\varphi)}{\cos(\varphi)\sin(\omega)}\end{array}\right\} \qquad (A.21)$$

being $\cos(\varphi)\ \sin(\omega) > 0$ and ψ and ξ the horizon angles defined by means of (A.1)-(A.3) and (A.12) respectively. Thus, the resulting horizon equations expressed in terms of ω and φ parameters are:

$$\begin{cases}\arccos(\cos(\varphi)\cos(\omega)) = \ \xi \in\ ]0, \pi[\quad\rightarrow \arccos(\cos(\varphi)\cos(\omega)) - \xi = 0\\[6pt]\arctan\left(\dfrac{-\sin(\varphi)}{\cos(\varphi)\sin(\omega)}\right) = \ \psi \in\ ]-\pi/2, \pi/2[\ \rightarrow \arctan\left(\dfrac{-\sin(\varphi)}{\cos(\varphi)\sin(\omega)}\right) - \psi = 0\end{cases} \quad (A.22)$$

A.3. Obtaining from the horizon an initial solution of the camera orientation parameters

We can use (A.21) to find an initial estimation of the angles $\{\omega, \varphi\}$ that define the orientation of the camera. If we compute the solution of the system (A.21), we obtain:

$$sin^2(\varphi) = \frac{1 - \cos^2(\xi)}{1 + \dfrac{1}{\tan^2(\psi)}}$$

Moreover, it is important to avoid numerical errors when $\tan(\psi)$ is close to zero due to $1/\tan(\psi)^2 \sim \infty$ so we use the following expression to compute φ:

$$sin^2(\varphi) = \frac{1 - \cos^2(\xi)}{\dfrac{\tan^2(\psi) + 1}{\tan^2(\psi)}} = \frac{\tan^2(\psi)\ \sin^2(\xi)}{\tan^2(\psi) + 1} \quad (A.23)$$

Because $0 \leq \sin^2(\xi) \leq 1$, we then confirm that $0 \leq \frac{\tan^2(\psi)\ \sin^2(\xi)}{\tan^2(\psi)+1} \leq 1$, having finally defined the next mathematical expression for angle φ:

$$\sin(\varphi) = \pm\sqrt{\frac{\tan^2(\psi)\ \sin^2(\xi)}{\tan^2(\psi)+1}} = \pm\sqrt{\sin^2(\xi)\sin^2(\psi)} = \pm\ |\sin(\xi)\sin(\psi)| \qquad (A.24)$$

Focusing on to the first equation of (A.21), the angle ω can be expressed as:

$$\cos(\omega) = \pm\sqrt{\frac{\cos^2(\xi)(\tan^2(\psi)+1)}{1+\cos^2(\xi)\tan^2(\psi)}} = \pm\frac{|\cos(\xi)|}{\sqrt{\cos^2(\psi)+\cos^2(\xi)\sin^2(\psi)}} \qquad (A.25)$$

Taking into account the relations between $\{\omega, \varphi\}$ and $\{\psi, \xi\}$ proven in (A.19) and (A.20), the next formulas involve all the possible situations in which these two angles can interact in terrestrial photography:

$$\begin{cases}\varphi = -\arcsin(\sin(\xi)\sin(\psi));\ \varphi \in\ ]-\pi/2, \pi/2[\\[6pt]\omega = \ +\arccos\left(\dfrac{\cos(\xi)}{+\sqrt{\cos^2(\psi)+\cos^2(\xi)\sin^2(\psi)}}\right);\ \omega \in\ ]0, \pi[\end{cases} \qquad (A.26)$$

Furthermore, regarding the initial value for the third angle κ, this can be approximated in accordance with the direction in which the photo is pointing. The methodology implemented in C-Pro allows the user to choose the quadrant between cardinal points where the principal camera axis seems to point and associates that with a proposed angular value. Therefore, angle κ is initialized as:

$$\begin{cases}if\ photo\ points\ between\ North\ and\ East \rightarrow\ \kappa = -\pi/4\ ;\\ if\ photo\ points\ between\ South\ and\ East \rightarrow\ \kappa = -3\pi/4\ ;\\ if\ photo\ points\ between\ North\ and\ West \rightarrow\ \kappa = \pi/4\ ;\\ if\ photo\ points\ between\ South\ and\ West \rightarrow\ \kappa = 3\pi/4\ ;\end{cases} \qquad (A.27)$$

References

Aarninkhof, S.G.J., Turner, I.L., Dronkers, T.D.T., Caljouw, M., Nipius, L., 2003. A video-based technique for mapping intertidal beach bathymetry. Coast. Eng. 49, 275–289. doi:10.1016/S0378-3839(03)00064-4.

Abdel-Aziz, Y.I., Karara, H.M., 1971. Direct linear transformation from comparator coordinates into objects space coordinates in close-range photogrammetry. In Proceedings of the symposium on close-range photogrammetry; pp. 1-18. Urbana, IL: American Society of Photogrammetry.

Almonacid-Caballer, J., Sánchez-García, E., Pardo-Pascual, J.E., Balaguer-Beser, A.A., Palomar-Vázquez, J., 2016. Evaluation of annual mean shoreline position deduced from Landsat imagery as a mid-term coastal evolution indicator. Mar. Geol. 372, 79–88. doi:10.1016/j.margeo.2015.12.015.

Andriolo, U., Sanchez-Garcia, E., Taborda, R., 2016. Using surfcam online streaming images for nearshore hydrodynamics characterization. 4as Jornadas de Engenharia Hidrográfica, Lisbon, Portugal. ISBN. 978-989-705-097-8; pp. 377-380.

Archetti, R., Schiaffi, C.F., Ferrari, M., Brignone, M., Rihouey, D., 2008. Video systems for coastal monitoring. Pranzini, E., Wetzel, L. (Eds.). Beach Eros. Monit. Beachmed-e/OpTIMAL Proj. 101–109.

Bacakoglu, H., Kamel, M.S., 1997. A three-step camera calibration method. IEEE transactions on instrumentation and measurement, Vol. 46, No. 5, 1997, pp. 1165-1172.

Boak, E.H., Turner, I.L., 2005. Shoreline Definition and Detection: A Review. J. Coast. Res. 214, 688–703. doi:10.2112/03-0071.1.

Bouguet, J.Y., 2015. Camera Calibration Toolbox for Matlab. Available at: http://www.vision.caltech.edu/bouguetj/calib_doc/.

Bracs, M.A., Turner, I.L., Splinter, K.D., Short, A.D., Lane, C., Davidson, M.A., Goodwin, I.D., Pritchard, T., Cameron, D., 2015. Evaluation of Opportunistic Shoreline Monitoring Capability Utilizing Existing "Surfcam" Infrastructure. J. Coast. Res. doi:10.2112/JCOASTRES-D-14-00090.1.

Brignone, M., Schiaffino, C.F., Isla, F.I., Ferrari, M., 2012. A system for beach video-monitoring: Beachkeeper plus. Comput. Geosci. 49, 53–61. doi:10.1016/j.cageo.2012.06.008.

Chandler, J., Fryer, J., Jack, A., 2005. Metric capabilities of low cost digital cameras for close range surface measurement. Photogramm. Rec. 17, 1–16. doi:10.1111/j.1477-9730.2005.00302.x.

Cornall, T.D., Egan, G.K., 2004. Measuring horizon angle from video on a small unmanned air vehicle. In 2nd International Conference on Autonomous Robots and Agents.

Dai, F., Lu, M., Kamat, V.R., 2011. Analytical Approach to Augmenting Site Photos with 3D Graphics of Underground Infrastructure in Construction Engineering Applications. J. Comput. Civ. Eng. 25, 66–74. doi:10.1061/(ASCE)CP.1943-5487.0000072.

Davidson, M., Van Koningsveld, M., de Kruif, A., Rawson, J., Holman, R., Lamberti, A., Medina, R., Kroon, A., Aarninkhof, S., 2007. The CoastView project: Developing video-derived Coastal State Indicators in support of coastal zone management. Coast. Eng. 54, 463–475. doi:10.1016/j.coastaleng.2007.01.007.

Erdman, 1998. Erdman Video System, http://video-monitoring.com. (Accessed 2 March, 2016).

Heikkila, J., Silvén, O., 1997. A four-step camera calibration procedure with implicit image correction. Proc. IEEE Comput. Soc. Conf. Comput. Vis. Pattern Recognit. 1106–1112. doi:10.1109/CVPR.1997.609468.

Holland, K.T., Holman, R. a, Lippmann, T.C., Stanley, J., Plant, N., 1997. Practical Use of Video Imagery in Nearshore Oceanographic Field Studies - Oceanic Engineering, IEEE Journal of 22, 81–92.

Holman, R. a., Stanley, J., 2007. The history and technical capabilities of Argus. Coast. Eng. 54, 477–491. doi:10.1016/j.coastaleng.2007.01.003.

Holman, R., Sallenger, A., Lippmann, T., Haines, J., 1993. The Application of Video Image Processing to the Study of Nearshore Processes. Oceanography 6, 78–85. doi:10.5670/oceanog.1993.02.

1084   Horus, 2007. Horus System, http://www.horusvideo.com/. (Accessed 5 October, 2016).

1085   Jiménez, J. A., Osorio, A., Marino-Tapia, I., Davidson, M., Medina, R., Kroon, A., Archetti, R., Ciavola, P.,
1086   Aarnikhof, S.G.J., 2007. Beach recreation planning using video-derived coastal state indicators. Coast.
1087   Eng. 54, 507–521. doi:10.1016/j.coastaleng.2007.01.012.

1088   Kim, J., Lee, S., Ahn, H., Seo, D., Seo, D., Lee, J., Choi, C., 2013. Accuracy evaluation of a smartphone-
1089   based technology for coastal monitoring. Meas. J. Int. Meas. Confed. 46, 233–248.
1090   doi:10.1016/j.measurement.2012.06.010.

1091   Kosta, 2006. KOSTASystem by AZTI, http://www.kostasystem.com/. (Accessed 9 June, 2016).

1092   Ooi, T.L., Wu, B., He, Z.J., 2001. Distance determined by the angular declination below the horizon. Nature
1093   414, 197–200. doi:10.1038/35102562.

1094   Oreifej, O., Lobo, N., Shah, M., 2011. Horizon constraint for unambiguous UAV navigation in planar scenes.
1095   Proc. - IEEE Int. Conf. Robot. Autom. 1159–1165. doi:10.1109/ICRA.2011.5979586.

1096   Rodríguez, J., Martín, M.T., Herráez, J., Arias, P., 2008. Three-dimensional image orientation through only
1097   one rotation applied to image processing in engineering. Appl. Opt. 47, 6631–6637.
1098   doi:10.1364/AO.47.006631.

1099   Sánchez-García, E., Balaguer-Beser, A., Taborda, R., Pardo-Pascual, J.E., 2016. Modelling landscape
1100   morphodynamics by terrestrial photogrammetry: An application to beach and fluvial systems.
1101   International Archives of Photogrammetry, Remote Sensing and Spatial Information Sciences, 41,
1102   1175–1182. doi:10.5194/isprsarchives-XLI-B8-1175-2016.

1103   Sánchez-García, E., Pardo-Pascual, J.E., Balaguer-Beser, A., Almonacid-Caballer, J., 2015a. Analysis of the
1104   shoreline position extracted from Landsat TM and ETM+ imagery. International Archives of
1105   Photogrammetry, Remote Sensing and Spatial Information Sciences, 991–998.
1106   doi:10.5194/isprsarchives-XL-7-W3-991-2015.

1107   Sánchez-García, E., Pardo-Pascual, J.E., Balaguer-Beser, A., Almonacid-Caballer, J., 2015b. Monitorización
1108   de espacios costeros mediante un sistema fotogramétrico: C-Pro. XVI Congr. la Asoc. Española
1109   Teledetección "Teledetección Humed. y Espac. protegidos" 281–284.

1110   Schwendeman, M., Thomson, J., 2015. A Horizon-Tracking Method for Shipboard Video Stabilization and
1111   Rectification. J. Atmos. Oceanic. Technol., 32, 164-176. doi: 10.1175/JTECH-D-14-00047.1

1112   Seedahmed, G.H., Habib, A.F., 2002. Linear Recovery of the Exterior Orientation Parameters in a Planar
1113   Object Space. Int. Arch. Photogramm. Remote Sens. Spat. Inf. Sci. Volume XXX, 245–248.

1114   Taborda, R., Silva, A., 2012. COSMOS: A lightweight coastal video monitoring system. Comput. Geosci. 49,
1115   248–255. doi:10.1016/j.cageo.2012.07.013.

1116   Van Den Heuvel, F.A., 1998. 3D reconstruction from a single image using geometric constraints. ISPRS
1117   Journal of Photogrammetry and Remote Sensing, 53, 354–368. doi:10.1016/S0924-2716(98)00019-7.